Final Project Report

to the NASA SR&T Program

for NASA Grant NAG5-662

Project Title:

Remote Measurements of Upper Atmospheric Density and Temperature

Principal Investigator:

Jeng-Hwa Yee
Space Department
Applied Physics Laboratory
The Johns Hopkins University
Laurel, MD 20710

Project Summary

Under the support of NASA Grant NAG5-662, Dr. Jeng-Hwa Yee participated in a suborbital experiment. The campaign was designed to study the photochemistry of the mesosphere by observing simultaneously the airglow emissions with in-situ minor species number density profiles. The experiment was very successful and some preliminary results have already been reported in various scientific meetings. Two scientific papers are currently in the process of final preparation for submission for publication. In this final project report, we will first give a background description of the experiment and follow by the summaries of the scientific papers currently being prepared.

1.0 INTRODUCTION

One of the most fundamental properties of any atmosphere is its vertical structure because the characteristic macroscopic scale length is the atmospheric scale height, H(=kT/mg), which is much smaller than the characteristic horizontal scale lengths such as the radius of the Earth, R_e, or the Rossby radius of deformation. ~$(gH)^{1/2}/f$, associated with large scale fluid motions of the atmosphere, where f is the Coriolis parameter. The atmosphere is for all practical purposes an ideal gas and on horizontal scales greater than 100 km a low Mach number fluid in hydrostatic pressure balance in the vertical coordinate. Measurements of any two of the following properties: number density, n, temperature, T, and pressure, p, as a function of altitude provide a complete description of the vertical structure of the atmosphere.

In the upper atmosphere these basic states are controlled by processes that influence its chemical composition, thermal structure and dynamic behavior, i.e. the interplay of incoming solar radiation, photochemistry, thermal and non-thermal radiative emissions, turbulent and molecular diffusion, global circulation, and electro-dynamical processes. The balance of these processes leads to the basic thermal structure of the atmosphere: the stratosphere, mesosphere, and thermosphere.

The successful launches of the Atmosphere Explorers (AE), Dynamics Explorer (DE) and Solar Mesosphere Explorer (SME) satellites have led to advances in our understanding of the upper thermosphere and to a lesser extent the mesosphere and the lower thermosphere. "*It is known that the global structure of this region of the atmosphere can be perturbed during stratospheric warmings and solar-terrestrial events (magnetospheric substorms, solar flares), but the overall structure and dynamics responses to these effects and even the basic controlling physical and chemical processes of these effects are not understood*" *(The Space Science Board of the Academy of Sciences).* This important region of the atmosphere has been the subject of a number of recent studies by theoretical modeling work, ground-based (NSF's CEDAR Campaign) and other suborbital measurements, and will be the main focus of the upcoming NASA Thermosphere-Ionosphere-Mesosphere, Energetics and Dynamics (TIMED) mission.

The Michigan Airglow Payload (MAP) rocket program, under the supervision of Dr. William Sharp at the University of Michigan, has been one of the suborbital programs supported by NASA through the years dedicated to the understanding of important chemical processes taking place in the mesosphere and lower thermosphere. The scientific payload on board the previous three MAP flights included an instrument devoted to the remote sensing of temperature and density of the atmosphere. The instrument, Near Infra-Red Spectrometer (NIRS), constructed under the support of Phillips Laboratory, is a 1/4 meter Ebert Spectrograph using charge-couple devices (CCD) as its detector. Using the remote sensing capabilities of NIRS to obtain limb-viewing spectral brightness

measurements of several atomic and molecular band dayglow emissions, NIRS provides MAP experiment with measurements of:

(1) Altitude profiles of atmospheric temperature and density;
(2) Altitude profiles of the chemically active minor species such as $O(^1D)$ and O_3; and
(3) The solar EUV, MUV and FUV energy input.

NIRS is a well-developed instrument and the necessary data analysis and inversion techniques have been fully developed, implemented, and tested (as demonstrated in the next section). It is an integral part of the MAP payload and the measurements obtained by NIRS are particularly relevant to the objectives of the MAP experiments.

2.0 SCIENTIFIC OBJECTIVES AND SIGNIFICANT ASPECTS

The mesosphere and lower thermosphere (60-180 km) is a region characterized by complex and coupled radiative, chemical, dynamical, and NLTE processes. In the absence of dynamic forcings, the atmosphere is under radiative equilibrium with its thermal structure determined by the heating due to the absorption of incoming solar radiation and cooling due to outgoing infrared radiation. Different species are responsible for the local heating and cooling at different regions of the atmosphere. One of the important heating and cooling agents is ozone through its photolysis and infrared radiation at 9.6 μm. The concentration of ozone determines the magnitudes of the local heating and cooling rates. Consequently, a strong coupling between chemistry and energetics exists in the region manifested by the odd-oxygen and odd-hydrogen chemistry below 100 km and odd-nitrogen chemistry above. The major chemical processes in the upper part of the mesosphere and in the thermosphere, involve rapid interactions between the odd-oxygen (O, O_3) and odd-hydrogen (OH, H, HO_2) families. Most of the odd-oxygen exists in the form of atomic oxygen which, in the sunlit atmosphere, is in rapid photochemical equilibrium with ozone,

$$O + O_2 + M \longrightarrow O_3 + M$$
$$O_3 + h\nu \longrightarrow O + O_2$$
$$O + O_3 \longrightarrow O_2 + O_2 .$$

Total odd-oxygen in this region is, in turn, controlled by catalytic destruction reactions involving hydrogen free radicals,

$$O + OH \longrightarrow H + O_2$$
$$O + HO_2 \longrightarrow OH + O_2$$
$$O_3 + H \longrightarrow OH + O_2 .$$

The chemistry of odd-hydrogen in the mesosphere is very complex and these hydrogen radicals are produced primarily through the dissociation of water vapor by Lyman Alpha,

$$H_2O + h\nu \ (\lambda < 200 \text{ nm}) \longrightarrow H + OH$$

and its reaction with $O(^1D)$,

$$O(^1D) + H_2O \longrightarrow OH + OH.$$

Results from previous studies have shown that the abundance of ozone in the upper stratosphere and lower mesosphere exceeds that predicted from theoretical models by 30% in the lower mesosphere to almost a factor of 2 near the mesopause. *Consequently, comprehensive measurements of ozone, atomic oxygen, $O(^1D)$, molecular oxygen and free hydrogen radical, water vapor densities are vitally important in solving this perplexing problem.*

As described previously, temperature in the mesosphere is strongly connected to the ozone

distribution. For the region above 75 km, an increase in ozone concentration will lead to a local increase in the heating rate (Strobel, 1978). In a region where the atmosphere is in radiative equilibrium, an increase in the heating leads to an increased temperature, with a time lag of order of 1 day at 80 km (Brasseur et al., 1987). If one ignores this temperature-chemistry feedback mechanism, to the first order, increased temperature results in a lower kinetic rate coefficient for the O_3 formation reaction, $O + O_2 + M \rightarrow O_3 + M$, and higher rate coefficient for the O_3 destruction reaction, $H + O_3 \rightarrow OH + O_2$. The combination of the two leads to the inverse temperature dependence of ozone observed in the stratosphere and mesosphere by Aikin and Smith (1986). *Temperature thus is an important parameter for determining the kinetic rate coefficients of some chemical reactions involved in the odd-oxygen and odd-hydrogen chemistry.*

The MAP experiment was conducted over White Sands, New Mexico in the summer of 1991. Table 2.1 summarizes the instrumenation, the measurement parameters, the techiniques used, and the scientists responsible for the experiments. MAP science team is currently in the process of examining the chemical processes taking place in both the summer high and low latitudes from data collected over several experiments over the past few years. Two scientific papers are in the processes of final preparation for publication and they are summarized in the next section. The copies of the manuscripts are enclosed in the appendices.

Table 2.1 MAP instrumentation, measured parameters and measurement techniques

Instrument	Measurement	Technique	Principal Investigator
SARS-O	O density	Resonance Fluorescence	Dr. Sharp University of Michigan
SARS-H	H density	Resonance Fluorescence	Dr. Sharp University of Michigan
UVFPI	OH	Resonance Fluorescence	Dr. Sharp University of Michigan
TOI	O_3 density	photochemistry	Prof. Llewellyn University of Saskatchewan
NIRS	O_2 density N_2 density $O(^1D)$ density O_3 density Temperature	Photo-absorption Photochemistry Photochemistry Rotational structure	Dr. Yee Applied Physics Laboratory

3.0 Project Summary Report

3.1 Photochemistry in the Mesosphere

Paper Title: Odd Hydrogen and Odd Oxygen in the Mesosphere at Equinox: Measurements and a Model

Authors: W. E. Sharp, R. W. Goodwin (Space Physics Laboratory, University of Michigan)
E. J .Llewellyn (Institute of Space and Atmospheric Studies, Univ. of Saskatchewan),
R. G. Roble (High Altitude Observatory, NCAR)
C. Y. She (Department of Physics, Colorado State University)
G. E. Thomas (LASP, University of Colorado)
Jeng-Hwa Yee (Applied Physics Laboratory, Johns Hopkins University)

Status: Submitted to Journal of Geophysics Research 1994)

Abstract:

Simultanous measurements of the concentrations of atomic oxygen, atomic hydrogen, hydroxyl, and ozone along with the temrpetaure in the mesosphere/lower thermosphere at equniox for moderate solar activity conditions are reproted. Redundancy in the ozone and temperature measurements are shown to be consistent with each other. The new NCAR TIMED_GCM is run for the conditions of the experiment and its predictions are shown to be consistent with magnitude and vertical profiles of the data. THere is evidence of turbulance between 80 and 90 km. The total mixing ratio for hydrogen is found to be constant 7 ppm between 60 km and 100 km.

Note: A copy of the paper is attached.

3.2 Density and Temperature, Ozone and O(^{1}D) Measurement Techniques

Paper Title: The $O_2(^1\Sigma)$ Dayglow Emissions: Application to Upper Atmosphere Remote Sensing

Authors: Jeng-Hwa Yee (Applied Physics Laboratory, Johns Hopkins University)

Presentation: AGU 1992 Fall Meeting at San Fransisco

Status: 80 % complete (to be submitted to Geophysics Research Letters, 1995)

Abstract:

The O_2 Atmospheric band emission covers an altitude region between ~40 and ~200 km in the dayglow and between ~80 and 100 km in the nightglow. Because of its extended altitude coverage and bright signal, this emission band provide the best spectral feature ofr upper atmosphere remote sensing. In this paper, we concentrate on examining the photochemical processes leading to the production of $O_2(^1\Sigma)$ molecules, the characteristics of the O_2 Atmospheric band emissions, and its application to atmosphere remote sensing.

Note: A copy of the paper is attached.

Odd Hydrogen and Odd Oxygen in the Mesosphere at Equinox: Measurements and a Model

W. E. Sharp[1], R. W. Goodwin[1], E. J. Llewellyn[2], R. G. Roble[3], C. Y. She[4], G. E. Thomas[5], J. -H. Yee[6]

[1]Space Physics Research Laboratory
University of Michigan, Ann Arbor, MI 48104

[2]Institute of Space and Atmospheric Studies
University of Saskatchewan, Saskatoon, Sask., Canada S7N 0W0

[3]High Altitude Observatory
National Center for Atmospheric Research, Boulder, CO 80307

[4]Department of Physics
Colorado State University, Fort Collins, CO 80523

[5]Laboratory for Atmospheric and Space Physics
University of Colorado, Boulder, CO 80309-0590

[6]JHU/Applied Physics Laboratory
Laural, MD 20707-6095

ABSTRACT

Simultaneous measurements of the concentrations of atomic oxygen, atomic hydrogen, hydroxyl, and ozone along with the temperature in the mesosphere/lower thermosphere at equinox for moderate solar activity conditions are reported. Redundancy in the ozone and temperature measurements are shown to be consistent with each other. The new NCAR TIME-GCM is run for the conditions of the experiment and its predictions are shown to be consistent with the magnitude and vertical profiles of the data. There is evidence of turbulance between 80 km and 90 km. The total mixing ratio for hydrogen is found to be a constant 7 ppm between 60 km and 100 km.

INTRODUCTION

The hydrogen species play a major role in controlling the distribution of oxygen and ozone in the mesosphere. There are diurnal, seasonal, and solar cycle variations in the abundance of oxygen and ozone here, so it is important to understand the role played by the hydrogen species in controlling the distribution of these oxygen species. The reactive hydrogen, of course, comes from the photodissociation of water vapor a species which has diurnal, seasonal, and, perhaps, solar cycle variations. It has been known for some time that current photochemical models underestimate the observed abundance of ozone in the mesosphere(e.g., Allen and Delitsky, 1991).

Reported here are the first simultaneous measurements of concentrations of atomic oxygen, atomic hydrogen, hydroxyl, and ozone along with temperature and density obtained in the mesosphere/lower thermosphere. These measurements were obtained by rocket borne instrumentation which did both in-situ sampling and remote sensing overhead and on the limb. The payload carried an Attitude Control System (ACS) which allowed the payload to be pointed at different targets.

The instruments were launched from White Sands Missile Range (Latitude 32.4° N, Longitude 106.3° W) on September 6, 1991, in the afternoon when the solar zenith angle was 48°. At this time the $F_{10.7}$ flux was 166, the 81 day average was 192, and Ap was 14. The launch was preceded by several significant thunderstorms (heavy downpour and lightening strikes) which may have launched gravity waves into the upper atmosphere.

Finally, the data will be compared with the output of the TIME-GCM recently described by Roble and Ridley (1993) and run for the conditions of this experiment.

INSTRUMENTATION AND ANALYSIS TECHNIQUES

All of the instruments were calibrated before flight. When they were on the payload, the optical instruments were aligned to each other and to a solar sensor to a knowledge of 0.1° prior to installation of the payload on the motor. The dead band of the ACS was 0.25°. For a short period during the flight the pointing accuracy

was updated by aligning the roll and pitch axes with the sun using a solar sensor which fed back an alignment error signal to the ACS.

Resonance scattering is the technique used to measure the atom concentrations. The instruments carry their own source of resonant radiation. The oxygen instrument uses the resonant 1304Å multiplet radiation created in a discharge lamp to scatter off the atmospheric oxygen whereupon it is scattered back to a photometer with a 1304Å filter. The hydrogen instrument uses the resonant 1216Å radiation created in the discharge lamp to scatter off the atmospheric hydrogen whereupon it is scattered back to a photometer with a 1216Å filter. The two instruments are deployed together on a boom to a distance of about one meter from the payload. Of importance here is that the payload roll axis is aligned along the trajectory when transiting the mesosphere/lower thermosphere for air flow perpendicular to the scattering plane. The instrument description, laboratory calibration, and data analysis procedure are described in Sharp (1991) for the oxygen sensor and Sharp and Kita (1987) for the hydrogen sensor. The arguments for the boom technique are discussed in Sharp (1980). The count rates from these instruments are directly proportional to the atom densities when the laboratory calibration is applied.

The data points in figure 1 show the measured atomic oxygen, [O], on the downleg. The upleg is identical above 78 km. There is no data below this because the experiment had not yet been deployed. The error bars represent the $\pm 1\sigma$ counting statistics. Note the wave like structure in the data below 90 km. The variation exceeds the counting statistics, so is real. The variation has an apparent wavelength of about 5 km which has been commented upon before (Sharp, 1991). The data points in figure 2 show the atomic hydrogen, [H], data. To reduce some of the fluctuations in the data a 7 point boxcar average of the flight data has been done. This is what is plotted so that every 7th point is independent of the others. This represents a 5 km smoothing of the data. Near the peak density at 82 km the count rate was about 650 Hz on a geocoronal background of 4900 Hz. The error bars are $\pm 1\sigma$ in the counting statistics. Where there is no bar the error is as large as or larger than the density determination at that point. There appears to be structure in the data particularly near 100 km. The smoothing may have masked finer structure such as is evident in the oxygen data.

Ozone is determined by monitoring the radiation from the O_2 Infrared Atmospheric 0,0 band at 1.27μm which results from the photolysis of ozone. This is a technique applied very successfully by the Solar Mesosphere Explorer team (Thomas, et al., 1984). The filter photometer used has an uncoated lead sulfide photodiode that measures the overhead emission rate as the payload traverses the mesosphere. The description of the instrument is given in Evans, et al. (1988) and was calibrated at the Space Physics Research Laboratory before flight. The procedure to deduce the ozone was to construct a model of the emission using the mechanisms responsible for the excited state (Mlynczak, et al., 1993), calculate the emission rate, integrate it with altitude and compare with the data. A September climatological ozone density distribution (Keating, et al., 1989) was the initial input. Small adjustments in this ozone distribution were made until a minimum error between model and the optical data occurred. The nature of this approach to the data analysis and the presence of a significant background precluded a deduction of ozone above 95 km. This fit to the emission rate data is shown in figure 3. The data exceeds the model calculations below 65 km because this was just after the nose cone came off and the payload hadn't come under the stable control of the ACS. By 65 km the photometer was viewing the same point on the celestial sphere. The error on the data represents the calibration of the instrument. The solid circles in figure 4 show the ozone which gave the fit to the emission data. The mean deviation of this profile from the September climatological was 10%.

Hydroxyl density was determined by viewing the solar resonance fluorescence radiation scattered by hydroxyl on the earth's limb using an ultraviolet pressure scanning Fabry-Perot interferometer coupled to a fixed grating spectrometer. The system resolution was 0.1Å. The instrument passed only a 1Å interval including three overlapping hydroxyl rotational lines at 3082.5Å, the $P_{11}(1)+Q_{11}(3)+P_{21}(3)$ lines. The instrument, its calibration and results from an initial flight have been described by Cageao (1989). The sensitivity of the instrument from laboratory calibrations was lower than expected, resulting in a very low count rate. Therefore, the limb data between 62 km and 82 km were summed together. The data points in figure 5 are this sum. A pure Rayleigh scattering spectrum was calculated using the high resolution solar flux measurements of Kurucz, et al. (1984). This spectrum was convolved with the instrument function to produce a synthetic background spectrum. To account for the line emission, the instrument function

was also added to the scattered spectrum at the point in pressure where the line emission was expected to be. The line emission fit was then adjusted until the data was fit. The solid line is the result while the dashed lines indicate the Rayleigh component and the line component. The product of the area under the line component and the emission rate "g-factor" (Fennelly, et al., 1989) gives the average OH column emission rate. This average column emission rate is shown in figure 6.

An ultraviolet imaging photopolarimeter (PMCE) obtained limb data on the Rayleigh scattering, and hence temperature and density. This instrument images the limb vertically onto a 128 element Reticon through a baffle system, an off axis parabolic mirror, a filter and an image intensifier. The filter wheel contained four filters having three at 2650Å with polarizer axis perpendicular, parallel, and 45° to the horizon and one at 1950Å with no polarizer. Figure 7 shows the total intensity obtained from the summation of the parallel and perpendicular data for the image at 2650Å. The radiance above 110 km is due to the nitric oxide, NO, gamma band resonance scattering of sunlight, while below 70 km there is modification to the Rayleigh scattered profile due to ozone absorption. The solid line is a model calculation which uses the September climatological density and temperature (Barnett and Gorney, 1985), a nitric oxide profile described by Barth (1989) from SME data taken in a similar part of the solar cycle using emission g-factors from Eparvier and Barth (1992), and an ozone profile that is given in figure 4. Between 70 km and 90 km the scattered light profile is proportional to the total density. Possession of an atmospheric density profile allows the determination of the temperature assuming hydrostatic equilibrium (Clancy and Rusch, 1989). The temperature determined at the limb point in this case is shown in figure 8.

(DATES)

A near infrared CCD spectrograph obtained data on the 0,0 and 0,1 Atmospheric bands from O_2 at 7620Å and 8640Å, respectively. The instrument, its calibration, and data analysis procedure have been described by Hays, et al., (1991). The inverted 0,1 band intensity shape and the optically thin 0,0 band shape give the temperature. The ratio of the 0,0 to 0,1 band inverted intensity gives the O_2 density where the 0,0 band becomes optically thick. This is the case for altitudes above 50 km when measurements are made on the limb where the slant path is long. Figure 8 shows the temperature determined from the 0,0 band when viewing vertically, where there is no self absorption by the 0,0 band. Figure 9 is the volume

emission rate of the 0,0 band derived from the overhead column emission rate. The temperature and a climatological O_2 density is used in an analysis of the absolute intensity of the Atmospheric 0,0 band to yield the O_3 density using the chemistry discussed by Hays, et al. (1991). The O_3 deduced from this data is given in figure 4.

The field of view of the limb measurements had the tangent point over Northern Colorado (≈41°N). The Colorado State University sodium lidar (She, et al., 1992) made temperature measurements of the mesopause region, albeit at night, approximately nine hours after the rocket launch. The temperatures deduced from this experiment are also plotted in figure 8.

In summary, the data along the trajectory at 32°N are [O], [H], [O_3], and temperature while on the limb at about 41°N are [OH], [O_3], and temperature.

DISCUSSION

Roble and Ridley (1993) have recently moved the lower boundary condition of the TIE-GCM to 10 mb (30 km) and report the initial simulations for equinox at minimum solar activity levels. The model contains new physical and chemical processes which describe the mesosphere and upper stratosphere. This model was run for the higher level of solar activity appropriate for this experiment and the output is compared with the data. There was no special "tuning" of the gravity waves, tides or chemical reaction rates from what is described by Roble and Ridley. The solid line in figures 1, 2, 4, 6, and 8 represent the [O], [H], [O_3], slant column OH, and temperature, respectively.

An examination of figures 1 and 4 indicates that above 70 km the density of atomic oxygen exceeds that of ozone by over a factor of ten. Thus, above this altitude odd oxygen is essentially atomic oxygen. Below 70 km the concentrations of the two species begin to converge to each other. At 64 km the [O]/[O3] is about 2.5. If the trend of the atomic oxygen data follows the TIME model ten [O]/[O3] would be unity at 60 km.

Bevilacqua, et al. (1983) describe the mean September 1980 water vapor profile obtained by observations at Bear Lake, California, a latitude not too different from White Sands. The altitude region below 80 km is shown in figure 10. It should give a sense of the

water vapor content at this time of the year for the mid-latitude region. Figure 10 also shows the recent data reported by the HALOE instrument on UARS for September 30, 1992 (Russell, et al., 1993). Note that the profiles are very similar in spite of being obtained a decade apart in time. The TIME-GCM output is the solid line. The short fall in the model calculations below 70 km is likely a result of not enough turbulent mixing in the model.

The mixing ratio was found for each constituent by using the total volume number density which was an output of the TIME-GCM. The results are shown in figure 11 as a function of altitude for atomic oxygen and hydrogen. Of interest here is that between 75 and 82 km both atom concentrations are increasing. However, between 82 km and 85 km both profiles show nearly constant mixing ratio. This constant mixing ratio occurs again between 86 km and 88 km. It is likely that these two regions are regions of turbulance because of the uniform mixing.

The data in figure 12 for the hydrogen species suggests that the atomic hydrogen and water vapor mixing ratios near 0.006 mb would be equal to 1 ppm. The hydrogen data was examined in conjunction with the TIME model to find the total mixing ratio of hydrogen. The total hydrogen at all pressure levels was found.

$$\text{Total } H_2 = 0.5 \times [H] + [H_2O] + [H_2]$$

Here, any contribution of methane was ignored as being small, less than 10% total hydrogen above 0.2 mb, about 60 km (Liu and Donahue, 1974). The mixing ratio of H_2O at 0.2 mb was about 7 ppm. The mixing ratio of H at 0.0004 mb was about 7 ppm although there is considerable variation due to dynamics. There was less in between these pressure limits. If the missing amount is assumed to be molecular hydrogen, $[H_2]$, then the required amount to maintain a constant total mixing ratio is consistent with the quantity of H_2 deduced by Atreya, et al., (1976) from stellar occultation measurements. The prediction of the TIME-GCM is shown in figure 12 as a solid line and begins to depart from a constant mixing ratio in total hydrogen below 0.05 mb, about 75 km. It should be noted that when the global mean model (Roble, 1994) is run, the total mixing ratio begins to decrease from constancy above 75 km also. the data here would suggest that the culprit is H_2 which in the TIME model is a factor of two below that reported by Atreya, et al. (1976). Increasing H_2 by a factor of 2 provides the constant total hydrogen

as is shown by the dashed line. This problem in the model is currently under investigation.

We required the downward flux of oxygen atoms at the maximum of the oxygen profile to be balanced by the flux implied by the density of oxygen at this maximum, which was at 95 km for this experiment. The oxygen atom production above 95 km by the Schumann-Runge continuum was calculated. The O_2 photodissociation cross sections tabulated by Hudson (1971) were used in conjunction with the solar maximum fluxes reported by Mount, et al., (1980) and solar minimum fluxes reported by Rottman (1981) to calculate the photodissociation rate. The photodissociation rate appropriate for the experiment was then determined by a linear scaling between the extremes using the $F_{10.7}$ flux for the day of the experiment. The height integrated production above 95 km represents the downward flux of oxygen atoms at 95 km. A flux of 1.36×10^{12} $cm^{-2}s^{-1}$ was found. At the peak of the profile ($d[O]/dz = 0$) the flux can be set equal to

$$\text{Flux} = -K\,[O]\,\{1/H_{av} + 1/T(dT/dz)\}$$

where H_{av} is the atmospheric scale height there, T is the temperature and K is the eddy diffusion coefficient. At 95 km the $[O] = 3.0 \times 10^{11}$ cm^{-3}, T=180 K, $dT/dz = 2.1 \times 10^{-5}$ K/cm and the required eddy diffusion coefficient is 2.3×10^{6} cm^2 s^{-1}. If the temperature from the TIME-GCM is used, there is essentially little difference in the eddy diffusion coefficient. The coefficient is consistent with the summary of various experimental and theoretical deductions compiled by Hocking (1985).

CONCLUSIONS

The first comprehensive simultaneously obtained data set on [O], [O_3], [H], [OH], and Temperature in the mesosphere is reported. This was for a moderate level of solar activity during fall equinox time period. The total hydrogen was found to be consistent with a constant 7 ppm, provided the H_2 in the TIME-GCM was doubled. The maximum concentration of atomic oxygen at 95 km was found to be consistent with the downward oxygen atom flux at 95 km provided the eddy diffusion coefficient is near 2.3×10^{6} cm^2s^{-1} at that altitude. The new TIME-GCM was run for the conditions of the experiment and the modeled quantities agreed with the data reasonably well. There was

evidence that the gravity wave field was not quite right and more turbulent mixing below 70 km was required.

ACKNOWLEDGMENT

The research reported here was done at the University of Michigan under NASA Grants NGR 23-005-360 and NAG5-662, at Colorado State University under NSF Grant ATM90-01824, and at the University of Colorado under NRL N00014-93-1-G020. The National Center for Atmospheric Research is supported by the National Science Foundation. We appreciate the able support of Paul Buchanan and the Wallops Flight Facility team in the launching of the payload.

REFERENCES

Allen, M., and M. C. Delitsky, A test of odd-oxygen photochemistry using Spacelab 3 Atmospheric Molecule Spectroscopy observations, *J. Geophys. Res., 96*, 12883, 1991.

Allen, M., J. I. Lunine, and Y. L. Yung, The vertical distribution of ozone in the mesosphere and lower thermosphere, *J. Geophys. Res., 89*, 4841, 1984.

Atreya, S. K., T. M. Donahue, W. E. Sharp, B. Wasser, J. F. Drake, and G. R. Riegler, Ultraviolet stellar occultation measurement of the H_2 and O_2 densities near 100 km in the earth's atmosphere, *Geophys. Res. Lett., 3*, 607, 1976.

Barrett, J. J., and M. Gorney, *Middle atmosphere reference model derived from satellite data*, Middle Atmosphere Program Handbook, vol. 16, Edited by K. Labitzke, J. J. Barnett, and B. Edwards, pp 47, SCOSTEP Sec., Univ. of Illinois, Urbana, 1985.

Barth, C. A., *Reference models for thermospheric NO*, Middle Atmosphere Program Handbook, vol. 31, Edited by G. M. Keating, pp 126, SCOSTEP Sec., Univ. of Illinois, 1989.

Bevilacqua, R. M., W. J. Wilson, and P. R. Schwartz, Measurements of mesospheric water vapor in 1984 and 1985: results and implications for middle atmospheric transport, *J. Geophys. Res., 92*, 6679, 1987.

Cageao, R. P., *A measurement of hydroxyl in the daytime mesosphere*, Ph.D. Thesis, University of Michigan, 1989.

Clancy, R. T., and D. W. Rusch, Climatology and trends of mesospheric (58 - 90 km) temperature based upon 1982 - 1986 SME limb scattering profiles, *J. Geophys. Res., 94*, 3397, 1989.

DeMore, W. B., S. P. Sander, D. M. Golden, R. F. Hampson, M. J. Kurylo, C. J. Howard, A. R. Ravishankara, C. E. Kolb, and M. J. Molina, Chemical kinetics and photochemical data for use in stratospheric modeling, Evaluation #10, *JPL pub. 92-20*, Jet Propulsion Laboratory, California Institute of Technology, Pasadena, 1992.

Eparvier, F. G., and C. A. Barth, Self absorption theory applied to rocket measurements of the nitric oxide (1,0) gamma band in the daytime thermosphere, *J. Geophys. Res., 97*, 13723, 1992.

Evans, W. F. J., I. C. McDade, J. Yuen, and E. J. Llewellyn, A rocket measurement of the O_2 infrared Atmospheric (0-0) band emission in the dayglow and a determination of the mesospheric ozone and atomic oxygen densities, *Can. J. Phys., 66*, 941, 1988.

Fennelly, J. A., D. G. Torr, and M. R. Torr, OH $A^2\Sigma - X^2\Pi(0,0)$ band rotational line emission rate factors, *J. Geophys, Res., 94*, 5183, 1989.

Hays, P. B., J. -H. Yee, and V. J. Abreu, *Remote measurement of upper atmospheric density: instrument definition*, Final report PL-TR-92-2003, Air Force Phillips Laboratory, 1991.

Hedin, A. E., Extension of the MSIS thermospheric model into the middle and lower atmosphere, *J. Geophys. Res., 96*, 1159, 1991.

Hocking, W. K., *Turbulence in the altitude region 80-120 km*, Middle Atmosphere Program Handbook, vol. 16, Edited by K. Labitzke, J. J. Barnett, and B. Edwards, pp 290-304, SCOSTEP Sec., Univ. of Illinois, Urbana, 1985.

Hudson, R. D., Critical review of ultraviolet photoabsorption cross sections for molecules of astrophysical and aeronomic interest, *Rev. Geophys. Space Res., 9*, 305, 1971.

Keating, G. M., M. C., Pitts, and D. F. Young, *Ozone reference models for the middle atmosphere (new CIRA)*, Middle Atmosphere Program Handbook, vol. 31, Edited by G. M. Keating, pp 1-36, SCOSTEP Sec., Univ. of Illinois, 1989.

Kurucz, R. L., I. Furenlid, J. Brault, and L. Testerman, *Solar Flux Atlas from 296 to 1300 nm*, National Solar Observatory Atlas No. 1, National Solar Observatory, Sunspot, NM, 1984.

Liu, S. C., and T. M. Donahue, Realistic model of hydrogen constituents in the lower atmosphere and escape flux from the upper atmosphere, *J. Atmos. Sci., 31*, 2238, 1974.

Mlynczak, M. G. S. Solomon, and D. S. Zaras, An updated model for $O_2(a^1\Delta_g)$ concentrations in the mesosphere and lower thermosphere and implications for remote sensing of ozone at 1.27 μm., *J. Geophys. Res., 98*, 18639, 1993.

Mount, G. H., G. J. Rottman, and J. G. Timothy, The solar spectral irradiance 1200-2550Å at solar maximum, *J. Geophys. Res., 85*, 4271, 1980.

Rottman, G. M., Rocket measurements of the solar spectral irradiance during solar minimum, 1972-1977, *J. Geophys. Res., 86*, 6697, 1981.

Roble, R. G., Energetics of the mesosphere and thermosphere, *Chapman Conference on the Mesosphere and Lower Thermosphere*, Asilomar, 1993.

Roble, R. G., and E. C. Ridley, A thermosphere-ionosphere-mesosphere-electrodynamics general circulation model (TIME-GCM): Equinox solar cycle minimum simulations (30-500 km). *Geophys. Res. Lett.*, submitted 1993.

Sharp, W. E., Absolute concentrations of $O(^3P)$ in the lower thermosphere, *Geophys. Res. Lett., 7*, 485, 1980.

Sharp, W. E., The measurement of atomic oxygen in the mesosphere and lower thermosphere, *Planet. Space Sci., 39*, 613, 1991.

Sharp, W. E., and D. Kita, In-situ measurements of atomic hydrogen in the upper mesosphere, *J. Geophys. Res., 92*, 4319,1987.

She, C. Y., J. R. Yu, H. Latifi, and R. E. Bills, High spectral resolution lidar for mesospheric sodium temperature measurements, *App. Opt., 31*, 2095, 1992.

Strobel, D. F., M. E. Summers, R. M. Bevilacqua, M. T. DeLand, and M. Allen, Vertical constituent transport in the mesosphere, *J. Geophys. Res., 92*, 6691, 1987.

Thomas, R. J., C. A. Barth, D. W. Rusch, and R. W. Sanders, Solar Mesosphere Explorer near-infrared spectrometer: measurements of 1.27μm radiances and the inference of mesospheric ozone, *J. Geophys. Res., 89*, 9569, 1984.

Figure captions

Figure 1. The measured [O]. The error bars represent the counting statistics. The solid line is the TIME-GCM prediction for [O].

Figure 2. The measured [H] smoothed by a 7 point boxcar average of the original data. The error bars represent the counting statistics. Where there is no bar the error is equal to or greater than the density at that point. The solid line is the TIME-GCM model.

Figure 3. The overhead emission at 1.27μm from the O_2 Infrared Atmospheric 0,0 band (+). The solid line is the model emission calculated using the ozone of figure 4.

Figure 4. Ozone density deduced from the 1.27μm emission (o), the attenuation of the UV backscatter (•), and the Atm 0,0 band emission (x). The solid line is the TIME-GCM model.

Figure 5. The limb radiance data (-o-) from the ultraviolet Fabry-Perot interferometer for the spectral interval 3081.9Å and 3082.7Å (in pressure units) summed between 62 - 82 km. The total fit (—) includes Rayleigh scattered sunlight (---) and resonance fluorescence from the OH $P_{11}(1)+Q_{11}(3)+P_{21}(3)$ lines at 3082.5Å (-•-).

Figure 6. The calibrated area under the line emission from figure 5 divided by the "g-factor". The solid line is the slant column density deduced from the TIME-GCM model (see text).

Figure 7. Limb profile of the UV Rayleigh scatter data from the photopolarimeter (+). The data are the sum of the horizontal and perpendicular polarization channels which corresponds to the unpolarized radiance. Model radiance, solid line, is described in the text.

Figure 8. The temperature profile obtained by the Na Lidar measurement (+), the PMCE measurement (o), and the DATES measurement (•). The solid line is the TIME-GCM calculation.

Figure 9. The volume emission rate of the Atmospheric 0,0 band deduced from the measured overhead column emission rate by DATES.

Figure 10. Fall equinox water vapor profiles from the microwave measurements (o) of Bevilacqua et al. (1983) and the limb absorption measurements (•) of UARS/HALOE (Russell et al. 1993). The bars are the precision and the solid line is the TIME-GCM model.

Figure 11. The mixing ratio of [O], (+), and [H], (x).

Figure 12. The hydrogen species mixing ratio where (Δ) is [H], (o) is [H_2O] from microwave and (+) is [H_2O] from UARS/HALOE. The lines are the TIME-GCM calculation of the total hydrogen (—) and same with an increase in H_2 by a factor of 2 (---).

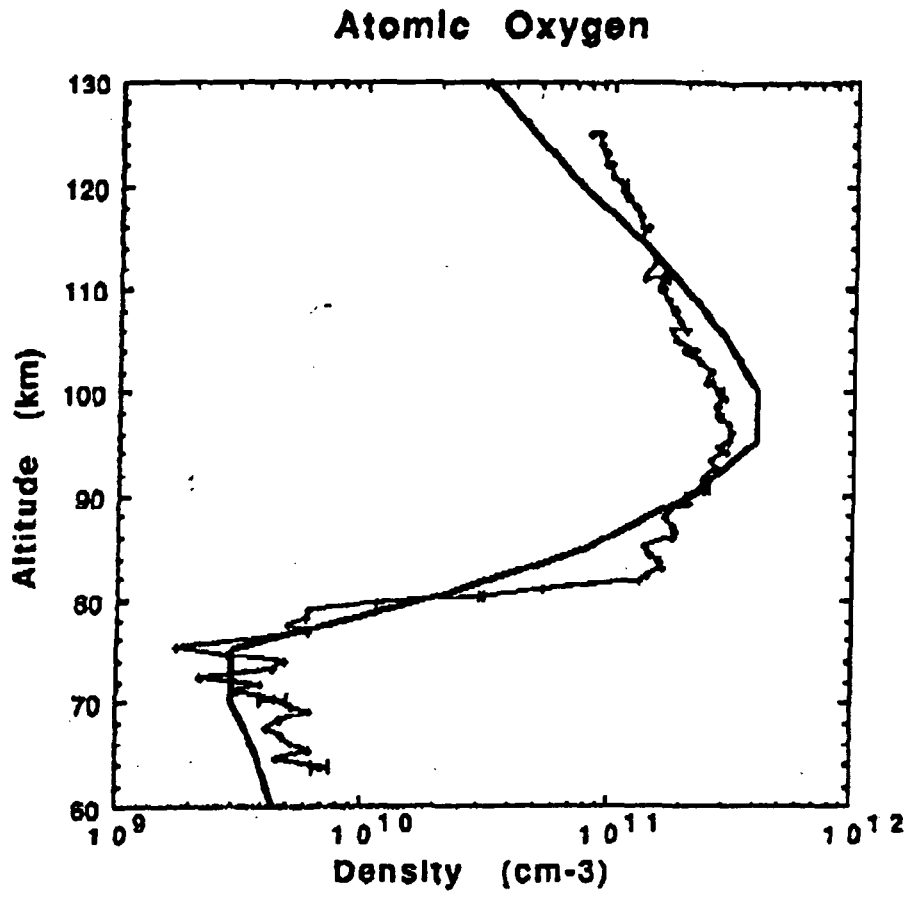
Atomic Oxygen
Altitude (km)
130
120
110
100
90
80
70
60
10^9
10^10
10^11
10^12
Density (cm-3)

fig 1

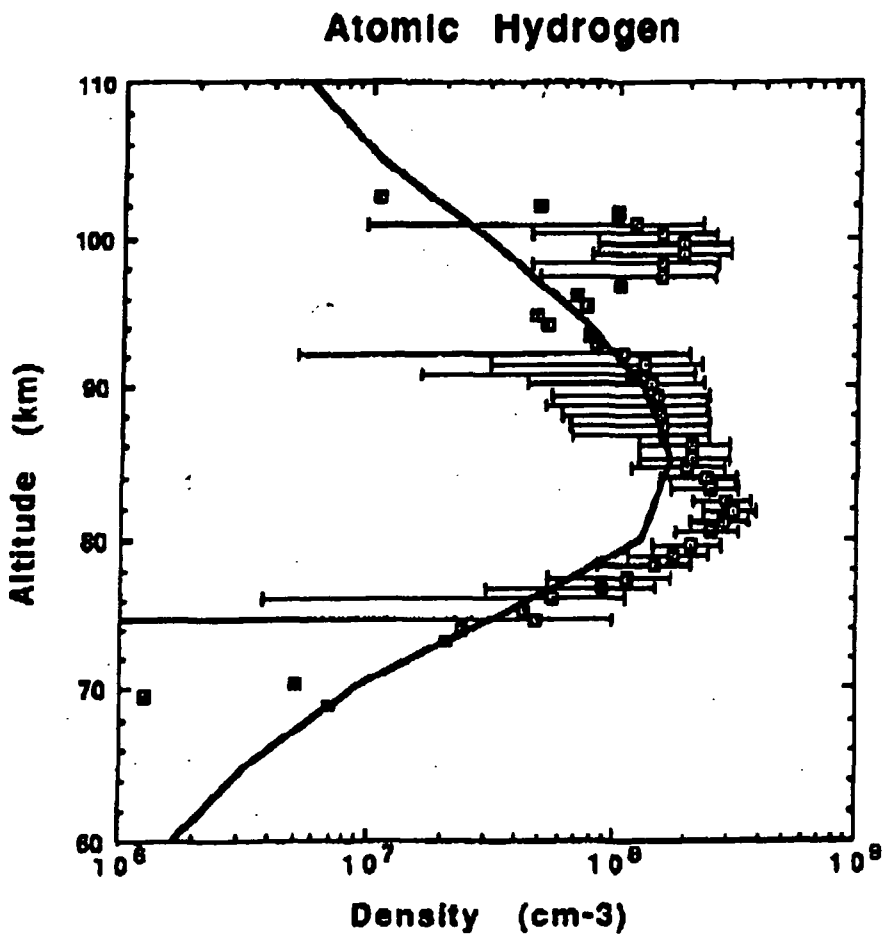
Atomic Hydrogen
110
100
90
80
70
60
Altitude (km)
10^6
10^7
10^8
10^9
Density (cm-3)

Fig 2

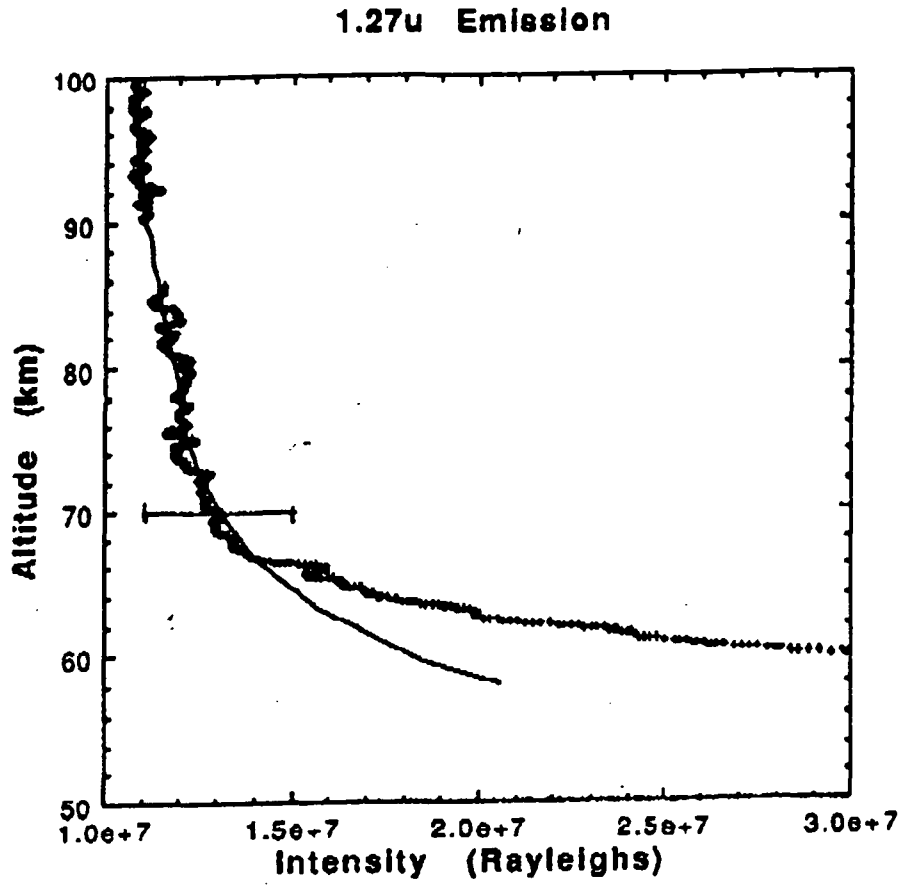
1.27u Emission
100
90
80
70
60
50
Altitude (km)
1.0e+7
1.5e+7
2.0e+7
2.5e+7
3.0e+7
Intensity (Rayleighs)

Fig. 3

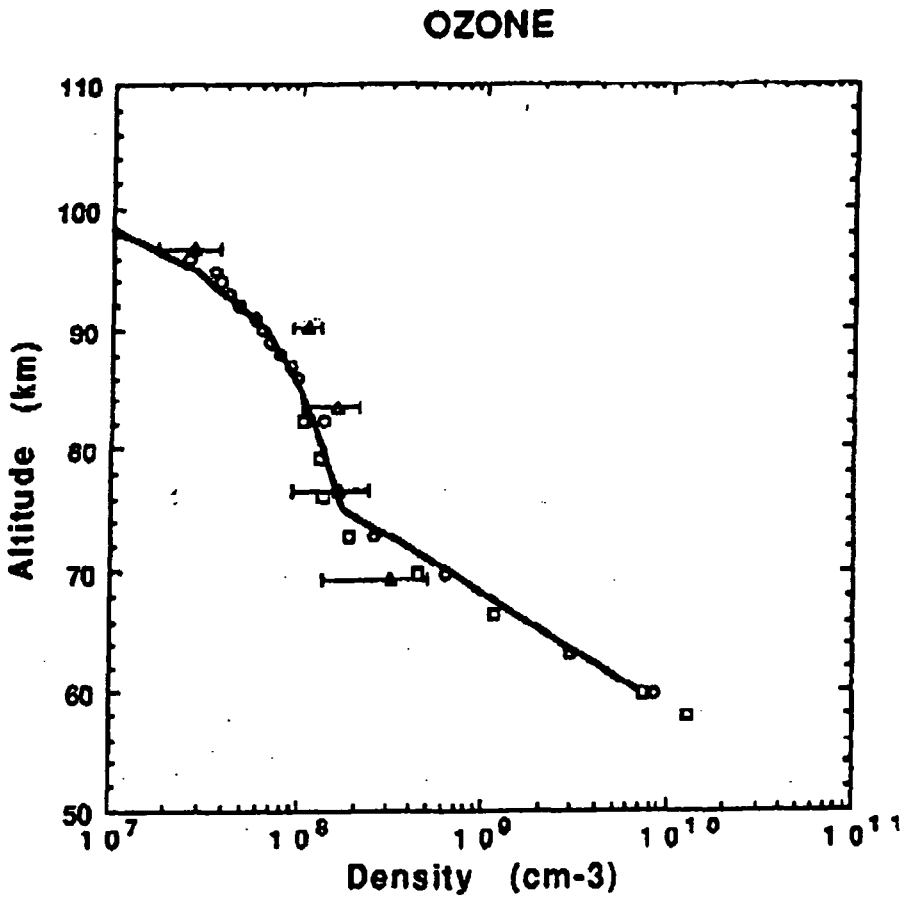
OZONE
110
100
90
80
70
60
50
Altitude (km)
10^7
10^8
10^9
10^10
10^11
Density (cm-3)

Fig 4

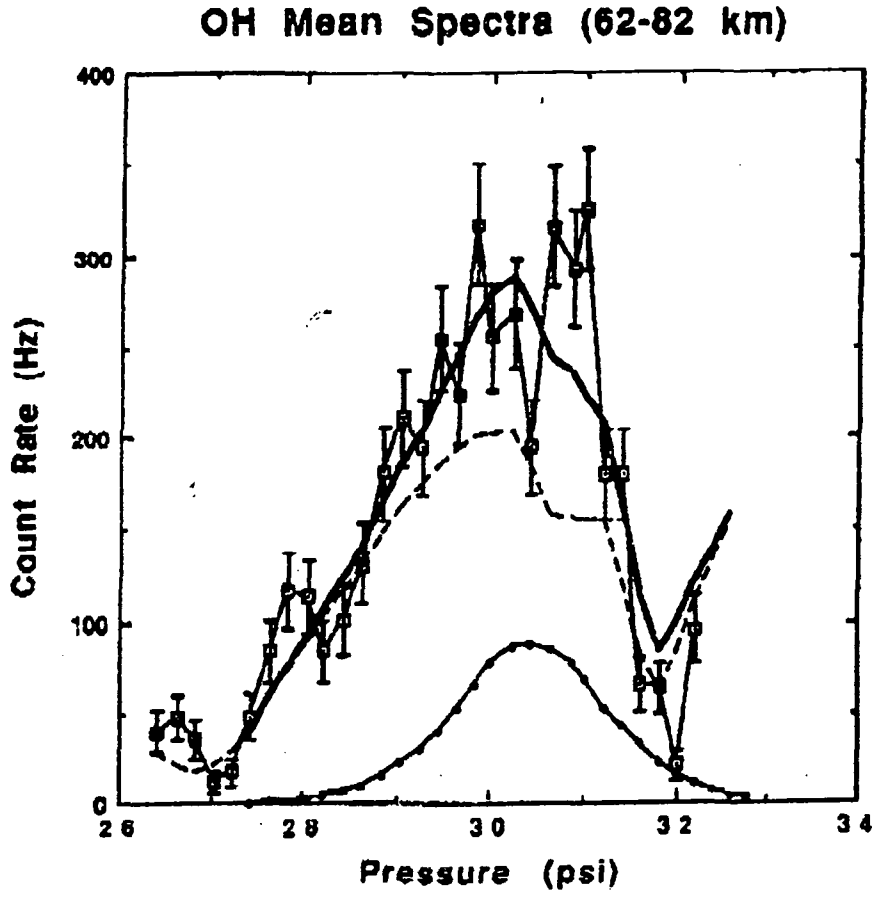
OH Mean Spectra (62-82 km)
Count Rate (Hz)
400
300
200
100
0
26
28
30
32
34
Pressure (psi)

fig 5

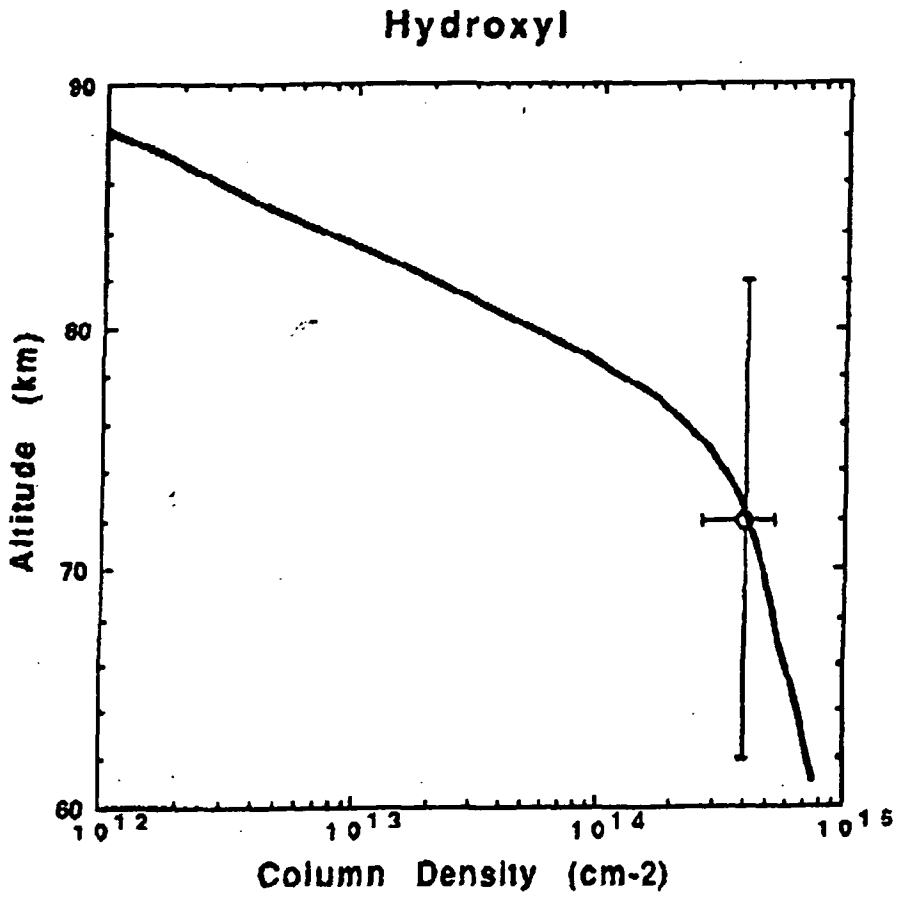
Hydroxyl
90
80
70
60
Altitude (km)
10^{12}
10^{13}
10^{14}
10^{15}
Column Density (cm-2)

fig 6

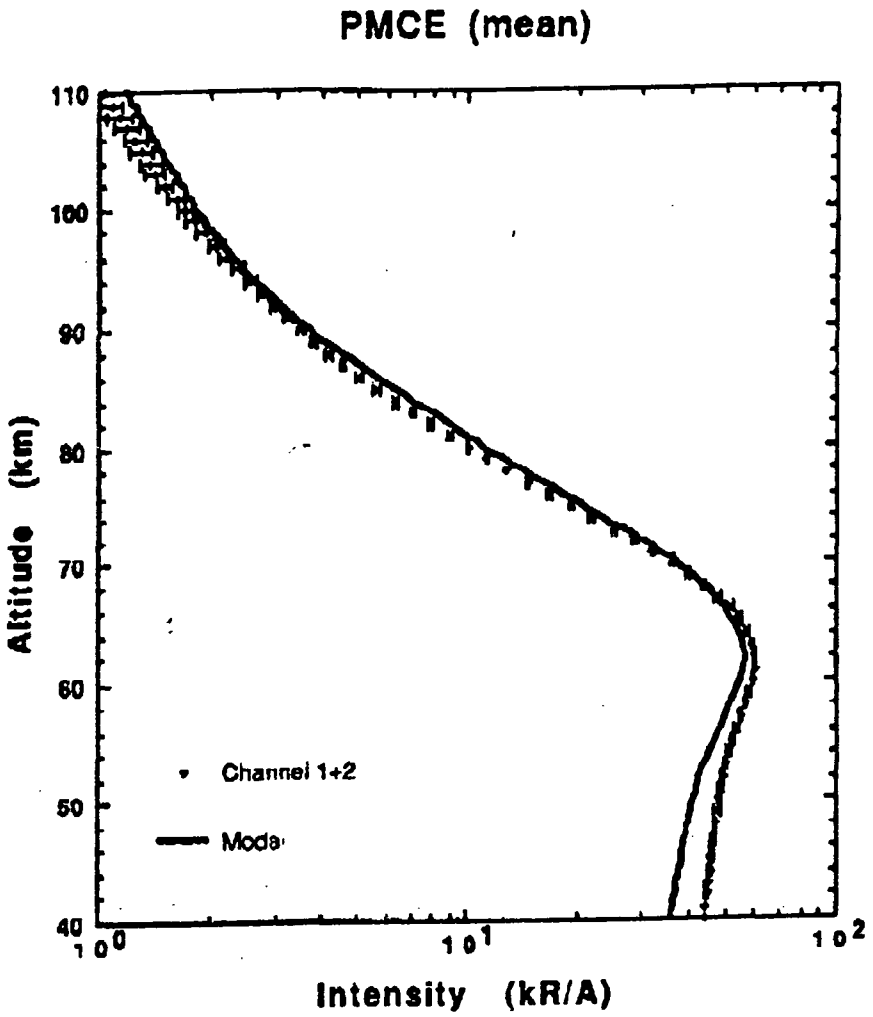
PMCE (mean)
Altitude (km)
110
100
90
80
70
60
50
40
Channel 1+2
Moda
10^0
10^1
10^2
Intensity (kR/A)

fig7

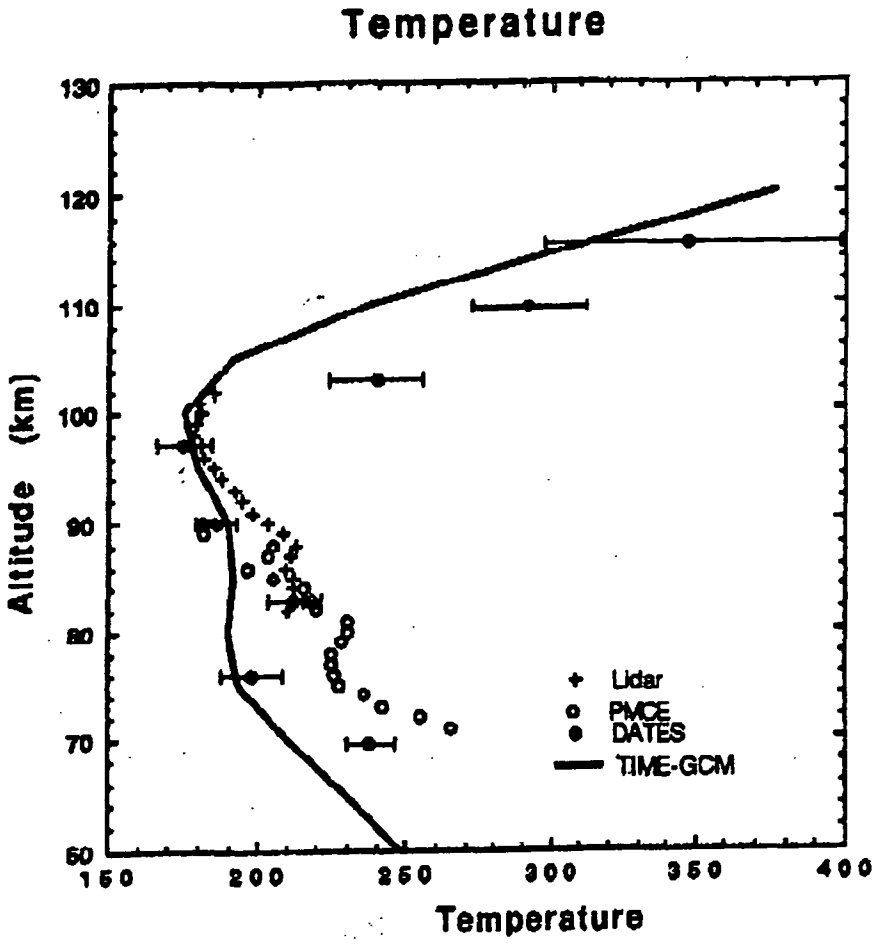
Temperature
Altitude (km)
130
120
110
100
90
80
70
60
150
200
250
300
350
400
Temperature
Lidar
PMCE
DATES
TIME-GCM

Fig 8

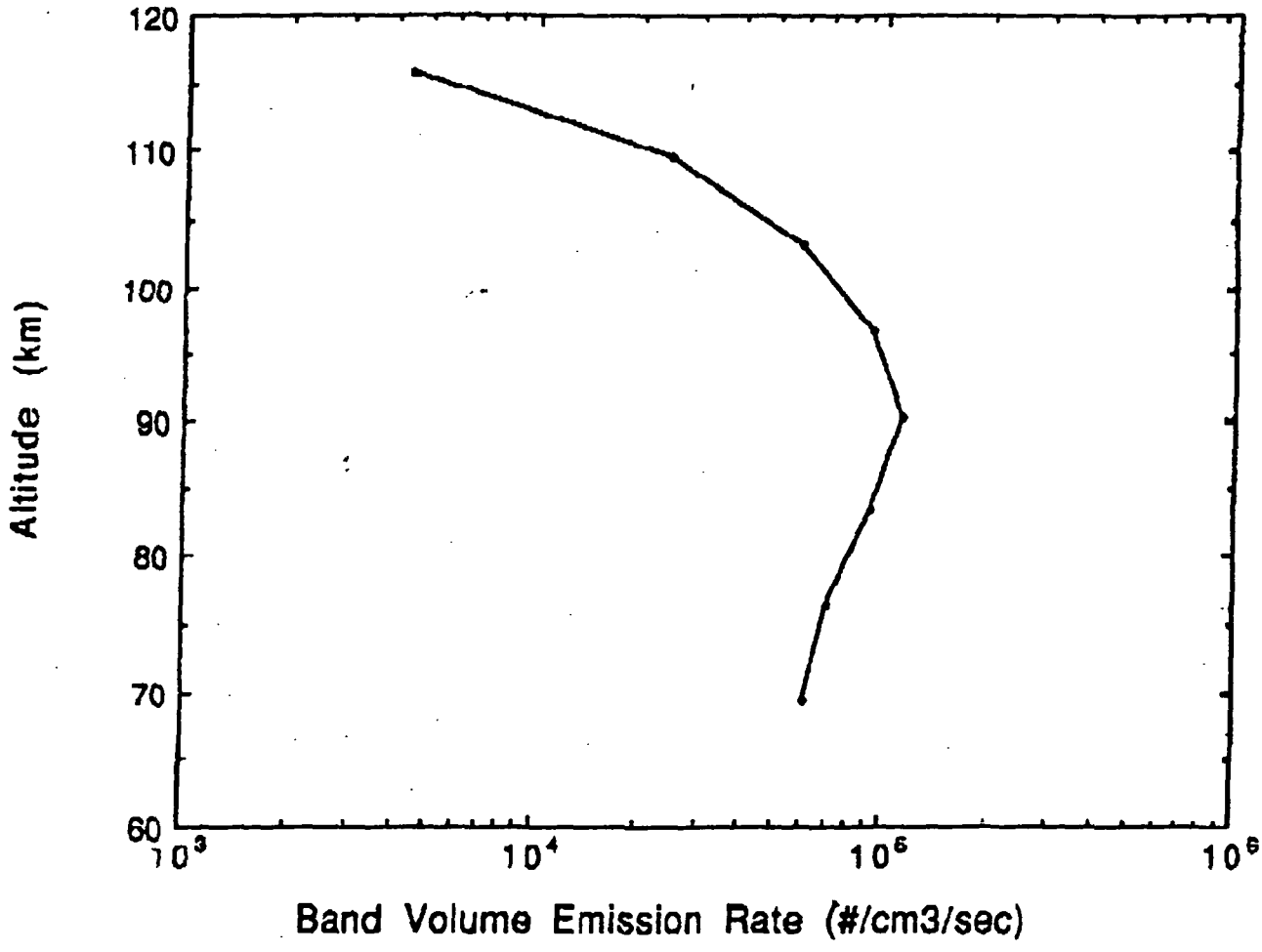
120
110
100
90
80
70
60
Altitude (km)
10³
10⁴
10⁵
10⁶
Band Volume Emission Rate (#/cm3/sec)

fig 9

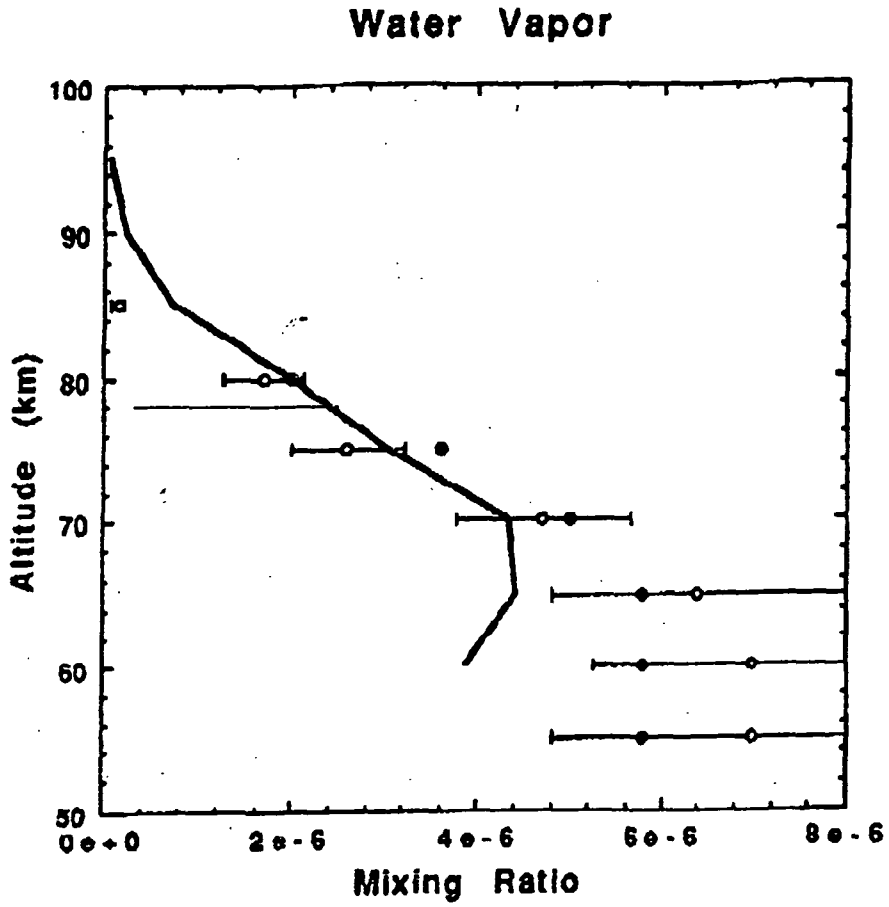
Water Vapor
100
90
80
70
60
50
Altitude (km)
0e+0
2e-6
4e-6
6e-6
8e-6
Mixing Ratio

Fig 10

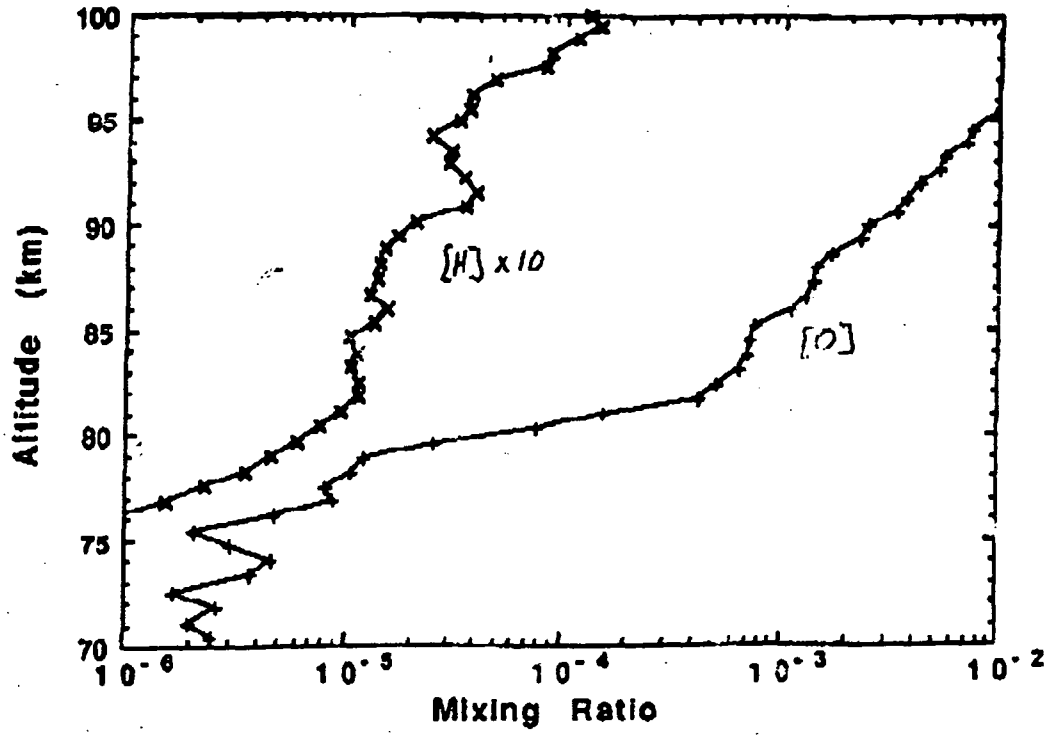
100
95
90
85
80
75
70
Altitude (km)
[H] x 10
[O]
10⁻⁶
10⁻⁵
10⁻⁴
10⁻³
10⁻²
Mixing Ratio

Fig 11

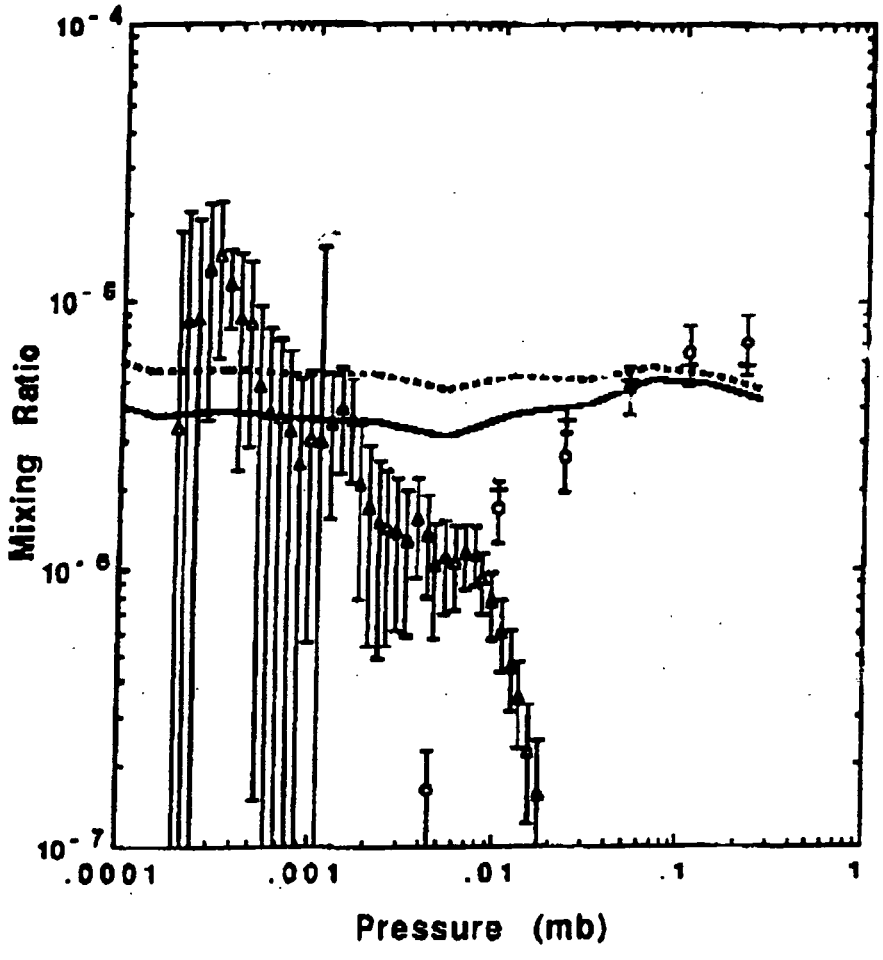

fig 12

The $O_2(^1\Sigma)$ Dayglow Emissions: Application for Upper Atmosphere Remote Sensing

Jeng-Hwa Yee

Applied Physics Laboratory
The Johns Hopkins University
Laurel, Maryland

To be Submitted to Journal of Geophysical Research, 1995

Abstract

The O_2 Atmospheric band emission covers an altitude region between ~40 km and 200 km in the dayglow and between ~80 and 100 km in the nightglow. Because of its extended altitude coverage and bright signal, this emission band provides the best spectral feature for upper atmosphere remote sensing. In this paper we concentrate on examining the photochemical processes leading to the production of $O_2(^1\Sigma)$ molecules, the characteristics of the O_2 Atmospheric band emissions, and its application to atmospheric remote sensing.

I. INTRODUCTION

The basic states of the upper atmosphere are controlled by processes that influence its chemical composition, thermal structure and dynamic behavior. These processes include the interplay of incoming solar radiation, photochemistry, thermal and non-thermal radiative emissions, turbulent and molecular diffusion, global circulation, and electro-dynamical processes. The successful launches of the Atmosphere Explorers (AE), Dynamics Explorer (DE) and Solar Mesosphere Explorer (SME) satellites have led to advances in our understanding of the upper thermosphere and to a lesser extent the mesosphere and the lower thermosphere. The spatial as well as temporal variabilities of wind, density and temperature in the mesosphere and lower thermosphere have been apparent for many years, being seen in limited sounding rocket, backscatter radar, and groundbased airglow data. The systematic variations that have been determined from these data sets are the obvious seasonal, latitudinal, and local time dependencies that are prescribed in the major models in use today. Our knowledge of the individual process in this region has reached a level of maturity that a sufficiently large and accurate morphological data base is needed in ordre to study the interplay of these processes. This global data base must rely on a sample technique that can provide measurements of the atmospheric wind, density, temperature and pressure with the consistency required to quantify the higher frequency variability. The only practical method of providing such global information is to use a remote sensing technique from space with an instrument that can provide the required accuracy and spatial sensitivity.

The O_2 Atmospheric band emission, originating in a transition between the excited $b^1\Sigma_g^+$ state and the ground $X^3\Sigma_g^-$ state of O_2, is one of the brightest emission features observed in the visible and near infra-red region of the airglow spectra. It covers an altitude region between ~40 km and 200 km in the dayglow and between ~80 and 100 km in the nightglow. Because of its extended altitude coverage and bright signal, the O_2 Atmospheric band emission provides the best spectral feature for upper atmosphere remote sensing.

The O_2 emission was first discovered from the ground by Meinel (1950) in the nightglow spectra shortly after the discovery of OH bands. Since then there has been an extensive set of groundbased observational data under nighttime and auroral conditions (see reviews of Meriwether, 1991). Among the whole O_2 Atmospheric system, the (0-0) band is expected to be the strongest. However, because the (0-0) band is completely absorbed

by the lower atmosphere and can only be observed from altitudes above the stratosphere, most of the ground-based measurements have been limited to the (0-1) band (Meinel, 1951; Chamberlain, et al, 1954; Wallace and Chamberlain, 1959, Yee et al., 1992, and many others). All of the (0-0) band observations were only made by instruments onboard rockets (Packer, 1961; Deans et al., 1976; Witt et al., 1979; McDade et al., 1986; Heller et al., 1987), Dynamics Explorer satellite (Skinner and Hays, 1985), the shuttle (Torr et al., 1986; Broadfoot, 1994).

It is currently believed that the $O_2(b^1\Sigma_g^+)$ molecules are produced in the upper atmosphere by three different mechanisms: (1) energy transfer from $O(^1D)$ to O_2; (2) direct solar fluorescence excitation; and (3) three-body recombination chemical reactions (Figure 1). The excited $O(^1D)$ atomsare produced by several different processes, depending on the altitude regions of the atmosphere. In the thermosphere above ~130 km the excited $O(^1D)$ atoms which are responsible for the $O_2(b^1\Sigma_g^+)$ production in the energy transfer reaction (mechanism 1), are mainly produced by the photoelectron impact on O and the dissociative recombination of O_2^+ ions (Soloman and Abreu, 1983). Between 80 and 130 km, the photodissociation of O_2 in the solar FUV Schumann-Runge continuum (SRC) and the solar Lyman-α (Ly-α) spectral regions become importance sources for the O(1D) atoms. The photolysis of O_3 by solar MUV photons in the Hartley bands also contribute below ~100 km . The direct

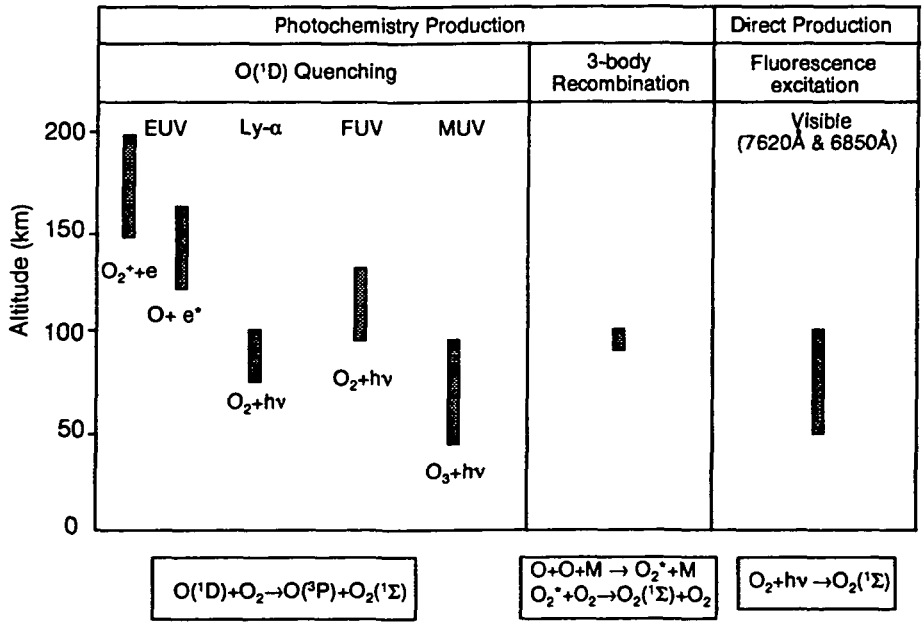

Figure 1. Production Mechanisms of $O_2(^1\Sigma)$ and their altitude regions of importance

excitation of $O_2(b^1\Sigma_g^+)$ from ground state $O_2(X^3\Sigma_g^-)$ by solar photons near 762nm and 690 nm (source 2) is important between 60 and 100 km. The chemical formation of $O_2(b^1\Sigma_g^+)$ by three-body recombination process is a minor source near 95 km during daytime, but it is the only source of $O_2(^1\Sigma)$ at night. In the mesosphere and lowe thermosphere, $O_2(^1\Sigma)$ is not completely quenched by collisions and radiates very strongly in the near-infrared (near ~760nm and ~860 nm). Consequently the emission rate of the O_2 Atmospheric band system contains information on the solar ultraviolet flux and the atmospheric composition, especially those species which are involved in the $O_2(^1\Sigma)$ photochemistry such as $O(^3P)$, $O(^1D)$, O_2, N_2, and O_3. Spectroscopically, the brightness and spectral line shape of each rotational line of this band system are affected by the atmospheric temperature (rotational Bolzmann factor and Doppler width) and wind profiles (Doppler shift). They are also strongly coupled to the O_2 density below 100 km for the (0-0) band through the self-absorption processes. Photochemically, the photolysis of O_2 and O_3 which leads to the production of $O(^1D)$ atoms releases significantly amount of chemical potential energy and atomic and molecular internal energy. The deposition of this energy largely determines the rate at which the atmosphere is heated (Mlynczak and Solomon, 1993). Consequently, the measurements of O_2 Atmospheric band system can provide a full description of atmospheric structure (i.e. density, wind, and temperature) of the mesosphere and lower thermosphere so that the thermodynamic response of this region to the time-varying sources of solar EUV, FUV and MUV radiation can be monitored. In addition, measurements of the local $O_2(^1\Sigma)$ volume emission rate can also be used to retrieve the concentrations of some chemically and radiatively active minor specices, such as the $O(^1D)$ and O_3 (Lopez-Gonzales et al., 1992, Yee et al., 1992, Yee et al., 1993) to study their roles in the photochemistry and energy budget.

This paper is the first of a series which discuss the remote sensing techniques that one can use to retrieve atmospheric state variables (i.e. winds, density, pressure, and temperature), energy input/heating rates (i.e. solar FUV and MUV input), and $O(^1D)$ and O_3 concentrations. In this paper we will concentrate on examining the photochemical processes leading to the production of $O_2(^1\Sigma)$ molecules, the characteristics of the O_2 Atmospheric band emissions, and its application to atmospheric remote sensing. We will outline the kinetic model used in the calculation of $O_2(^1\Sigma)$ concentrations in the daytime atmosphere and present theoretical formulations used to calculate the spectral brightness of any rotational line in the O_2 Atmospheric band system (Section 2). We will compare

our model results with previous experimental dayglow data from various geophysical conditions (i.e. solar activities, solar zenith angle, etc.). In addition, we have conducted four rocket campaigns during the last five years from White Sands, New Mexico and Poker Flat, Alaska. One of the instrument payload, the Density and Temperature Spectrograph (DATES), is designed to accurately measure the atmospheric O_2 density and temperature from the spectral characteristics of the O_2 band emissions. The description of the DATES instrument, its observational results, and their comparison with model calculation will be presented (Section 3). Finally, we will describe the application of O_2 Atmospheric band emissions to remote sensing of the terrestrial atmosphere (Section 4). It is beyond the scope of the current paper to present the detailed algorithms and inversion techniques for retrieving geophysical parameters from the spectral brightness measurements of the O_2 Atmospheric band system. The detailed inversion techniques will be presented in subsequent papers. These will include the recovery of (1) wind and temperature profiles from high resolution spectral line shape measurements of any rotational line in this band system, (2) atmospheric density and temperature profiles from spectral brightness measurements of O_2 (0-0) and (0-1) band emissions, and (3) $O(^1D)$ and O_3 number density profiles from a measured $O_2(^1\Sigma)$ volume emission rate profile. The techniques presented in these papers will be applied to measurements obtained by the High Resolution Doppler Imager (HRDI) flown on the Upper Atmosphere Research Satellite (UARS) (Hays et. al, 1992) and by the Density and Temperature Spectrograph (DATES) flown on the NASA Michigan Airglow Payload (MAP) rockets. The theoretical model presented in this paper will be the basis for the necessary algorithm development, inversion kernel determinations, and the error assessments for the subsequent work on upper atmospheric remote sensing.

2. THE O_2 ATMOSPHERIC BAND EMISSION

2.1 The $O_2(^1\Sigma)$ Photochemistry

The first detailed photochemistry study of $O_2(^1\Sigma)$ molecules in the daytime upper atmosphere between 40-130 km was reported by Wallace and Hunten (1968) based on the O_2 Atmospheric (0-0) and (0-1) band emission brightness measured from several rocket-borne photometers and spectrometers. In this classic paper, Wallace and Hunten (1968) presented what have become an accepted theory of the excitation mechanisms for the $O_2(b^1\Sigma_g^+)$ molecules: a fluorescence process in the region between 70 and 100 km and an energy transfer process from $O(^1D)$ to O_2, with the $O(^1D)$ atoms produced by O_2 photodissociation in the Schumann-Runge continuum above 100 km and by the O_3 photodissociation of ozone in the Hartley bands below 80 km. They also considered a direct production of $O_2(^1\Sigma)$ from ozone photolysis, which later was found to be ineffective (Gauthier and Snelling, 1970, 1971). A small three-body recombination or Chapman type chemical source was suggested near 90 km. This chemical source is responsible for the O_2 Atmospheric band emission observed in the nightglow and the reactions involved have been examined later by McDade et al. (1986) in the ETON rocket experiment.

The O_2 Atmospheric (0-0) and (1-1) band dayglow emissions above 150 km were first reported by Skinner and Hays (1985) from broadband Fabry-Perot measurements near 765 nm onboard the Dynamic Explorer (DE) satellite. Later Torr et al. (1986) reported their spectroscopic observation from experiments onboard Spacelab 1 and identified emission features which involve high vibrational levels of the $O_2(^1\Sigma)$ state, up to υ'=4. The υ' = 0, 1 of the $O_2(^1\Sigma)$ molecules at these altitudes are generated from the same $O(^1D)$ + O_2 energy transfer reaction taking place in the aurora and below 100 km in the dayglow (Slanger 1986). Torr et al. (1986) suggested the production mechanism of υ'=2-4 to be energy transfer between $N(^2D)$ and O_2. However, Slanger et al. (1987) later argued that this proposed mechanism needs to be further investigated by re-examining the observed spectra to include all other possible emission features present in the observed spectra. In this paper, we consider the $O(^1D)+O_2$ reaction to be the only source of $O_2(^1\Sigma)$ molecules in the thermosphere.

Table 1 lists the chemical and spectroscopic processes involved in the production and quenching of $O_2(^1\Sigma)$ molecules included in our study. The photochemical processes of

$O(^1D)$ atom and $O_2(^1\Sigma)$ molecule below ~130 km have been discussed in details by Mlynczak et al. (1993) in their recent paper on the $O_2(a^1\Delta_g)$ photochemistry. Except as noted in Table 1, we use rate constants adopted by Mlynczak et al. (1993) from the latest panel recommendation and evaluations. The production and loss processes of $O(^1D)$ atoms in the daytime thermosphere above 130 km have been examined previously by Solomon and Abreu (1986) through the 630nm dayglow emission. Here we only listed the two dominant sources, the photoelectron impact on O and dissociative recombination of O_2^+ ion.

Since the lifetime of the $O_2(^1\Sigma)$ molecule is very short (radiative lifetime of ~12 seconds), the transport of $O_2(^1\Sigma)$ is not important. When losses (i.e. radiation and quenching) are considered with production processes in a simple photochemical equilibrium steady state calculation, the contribution each production process makes to the total $O_2(^1\Sigma)$ number density as a function of altitude is,

$$[O_2(^1\Sigma)] = \frac{P_{DR} + P_{PE} + P_{SRC} + P_{Ly\text{-}\alpha} + P_{Hartley} + P_{FE} + P_{3\text{-}body}}{A_{O_2(^1\Sigma)} + Q_{N_2} + Q_{O_2} + Q_{O_3} + Q_O} \qquad (1)$$

Table 1. Kinetic and Spectroscopic Processes for the $O_2(^1\Sigma)$ chemistry

Process	Rate	Efficiency orQuantum	Reference
$O(^3P)+e^* \rightarrow O(^1D)+e$			Solomon and Abreu (1986)
$O_2^+ + e \rightarrow O(^1D) + O$			Solomon and Abreu (1986)
$O_2+h\nu \rightarrow O(^1D)+O$	SRC, J_∞=		
$O_2+h\nu \rightarrow O(^1D)+O$	Ly-α, $J_\infty=4.5\times10^{-9}$	$0.44 < \beta_1 < 1.0$	
$O_3+ h\nu \rightarrow O(^1D)+O_2$	Hartley, $J_\infty=8.1\times10^{-3}$	$\beta_2=0.9$	WMO(1985),JPL(1992)
$O(^1D)+N_2 \rightarrow O(^3P)+N_2$	$1.8\times10^{-11}\, e^{-110/T}$		JPL(1992)
$O(^1D)+O_2 \rightarrow O(^3P)+O_2(^3\Sigma)$	$3.2\times10^{-11}\, e^{-70/T}$	$1-\beta_{O_2(1_\Sigma)}=0.23$	
$\rightarrow O(^3P)+O_2(^1\Sigma,\upsilon'=0)$		$\beta_{O_2(1_\Sigma)}=0.77$,fo= 0.13,	
$\rightarrow O(^3P)+O_2(^1\Sigma,\upsilon'=1)$		$f_1=0.87$	
$O_2(^3\Sigma,\upsilon''=0)+h\nu \rightarrow O_2(^1\Sigma,\upsilon'=0)$	g_∞(762nm)=		DeMajistre and Yee (1995)
$\rightarrow O_2(^1\Sigma,\upsilon'=1)$	g_∞(689nm)=		
$O + O + M \rightarrow O_2^* + M$			See McDades et al. (1988)
$O_2^*+O_2 \rightarrow O_2(^1\Sigma)+O_2$			
$O_2(^1\Sigma,\upsilon')+ N_2 \rightarrow O_2(^3\Sigma) + N_2$	2.1×10^{-15}		JPL(1992)
$O_2(^1\Sigma, \upsilon')+ O_2 \rightarrow O_2(^3\Sigma) + O_2$	3.9×10^{-17}		JPL(1992)
$O_2(^1\Sigma, \upsilon') \rightarrow O_2(^3\Sigma)+ h\nu$	A_o=0.0833		

A_1=

where

P_{DR}: the production rate of $O_2(^1\Sigma)$ by energy transfer of $O(^1D)$ with O_2 following dissociative recombination of O_2^+ ion;

P_{PE}: the production rate of $O_2(^1\Sigma)$ by energy transfer of $O(^1D)$ with O_2 following photoelectron impact on O;

P_{SRC}: the production rate of $O_2(^1\Sigma)$ by energy transfer of $O(^1D)$ with O_2 following photodissociative of O_2 in the Schumann-Runge continuum;

$P_{Ly\text{-}\alpha}$: the production rate of $O_2(^1\Sigma)$ by energy transfer of $O(^1D)$ with O_2 following photodissociation of O_2 in the Lyman-α spectral region;

P_{FE}: the production rate of $O_2(^1\Sigma)$ by fluorescence excitation of O_2 at 762nm and 685nm;

$P_{Hartley}$: the production rate of $O_2(^1\Sigma)$ by energy transfer of $O(^1D)$ with O_2 following photodissociative of O_3 in the Hartley band;

$P_{3\text{-}body}$: the production rate of $O_2(^1\Sigma)$ by energy transfer of $O(^1D)$ with O_2 following photodissociation of O_2 in the Lyman-α spectral region;

$A_{O_2(1\Sigma)}$: the Einstein transition probability (~0.0833 sec^{-1}) of $O_2(^1\Sigma)$; and

Q_{N_2}, Q_{O_2}, Q_{O_3}, Q_O: quenching rate by N_2, O_2, O_3 and O respectively.

The production rate of $O_2(^1\Sigma)$ from energy transfer reaction of $O(^1D)$ with O_2, $P_{O(^1D)+O_2}$, such as P_{DR}, P_{PE}, P_{SRC}, $P_{Ly\text{-}\alpha}$, and $P_{Hartley}$, is related to the production rate of $O(^1D)$, $P_{O(^1D)}$, by

$$P_{O(^1D)+O_2} = \frac{\beta_{O_2(^1\Sigma)} k[O_2] P_{O(^1D)}}{A_{O(^1D)} + k_{O_2}[O_2] + k_{N_2}[N_2]}.$$

where $\beta_{O_2(^1\Sigma)}$ is the transfer efficiency between $O(^1D)$ and O_2 molecule, $A_{O(^1D)}$ is the Einstein transition probability of $O(^1D)$ atom, k_{O_2} and k_{N_2} are quenching rate coefficients of the $O(^1D)$ atoms by collisions with O_2 and N_2 respectively.

Figure 2 presents the calculated number density profile of $O_2(^1\Sigma)$ in the daytime upper atmosphere between 40 and 200 km under moderate solar activity (F10.7=150) at 0 degree solar zenith angle and its individual contribution from each of the production sources listed above. The $O(^1D)$ production rates in the thermosphere including all minor sources are calculated using the photochemical model of Solomon and Abreu (1984) and the solar EUV fluxes (scaled by F10.7) based on the Hinteregger reference spectra. The production rates of $O(^1D)$ atoms from photolysis of O_2 and O_3 are calculated using the

cross-sections and techniques described in JPL *Chemical Kinetics and photochemical data for use in stratospheric modeling* (1992). For photolysis of O_2, we used the reference FUV spectrum based on measurements of the Airglow Solar Spectrometer Instrument (ASSI) onboard San Marcos 5 satellite (Schmidtke et al., 1992) and the absorption cross-section measured by Wanahabe (1964). The production rate by fluorescence excitation by solar photons at 762nm (A band) and 689 nm (B band) are calculated using the technique described by DeMajistre and Yee (1995). The temperature and O, O_2, N_2 number density profiles are obtained from the MSIS-90 neutral atmosphere model (Hedin, 1990) at a time (noon on spring equinox) and geographic location (0° latitude and 0° longitude) where the solar zenith angle is very close to 0 degree. The O_3 number density profile is adopted from the MOTRAN(XXX). Note that the dominant source of the excited $O_2(b^1\Sigma)$ molecules between 90 and 140 km is the energy transfer reaction of $O(^1D)$ with O_2 following photodissociation of O_2 by solar radiation in the SRC spectral region (FUV). The dominant source below ~60 km is the similar energy transfer reaction following the photolysis of O_3. The fluorescence excitation mechanism is important between 60 and 90 km. It should be noted that the O_3 number density profiles between 50 and 90 km have shown to have large local time as well as seasonal variations (Zommerfelds et al., 1989; Thomas, 1990; Bevilacqua et al. 1990) and there is still

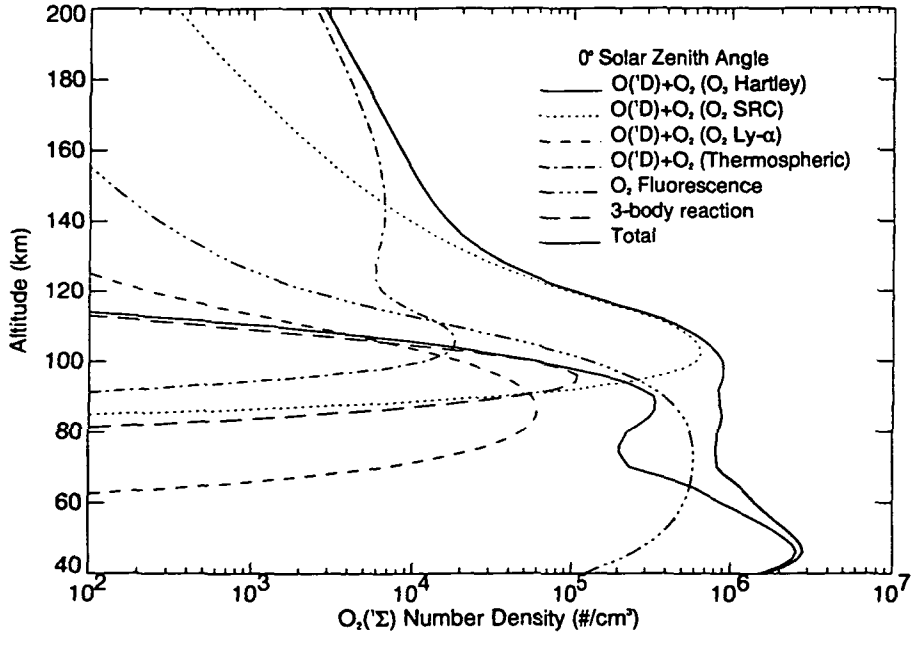

Figure 2. Calculated $O_2(^1\Sigma)$ number density profile at 0° solar zenith angle under moderate solar activity condition.

disagreement between the model and observations (Allen, 1984; Clancy et al., 1987). As a results, one should expect some degree of variations in the $O_2(^1\Sigma)$ density profile, especially below 60 km where the O_3 photolysis source dominates.

Figure 3 shows the calculated $O_2(^1\Sigma)$ number density profiles at 90° solar zenith angle under the same solar activity condition. The O_2 and O_3 absorption optical depths are calculated based on sun ray geometry and no variation of O_2 and O_3 densities with solar zenith angle is assumed. In fact, it is well known that O and O_3 undergo rapid interchange reaction in the mesosphere (Allen et al. 1984, Zommerfelds et al., 1989) and the concentrations of O and O_3 have noticeable diurnal variations especially during twilight. The detailed investigation on the solar zenith angle effect on the $O_2(^1\Sigma)$ concentration should take this variation into consideration. Here only the effect of increasing optical depth on the $O_2(^1\Sigma)$ production mechanism is demonstrated. The decrease in $O_2(^1\Sigma)$ concentration below ~70 km, consequently, results solely from the attenuation of solar MUV fluxes as the optical depth increases. The contributions from processes such as fluorescence excitation of O_2 and photolysis of O_2 and O_3 diminish their relative importance as the solar zenith angle increases and the three-body recombination source eventually becomes the only source of O_2 Atmospheric band airglow at night.

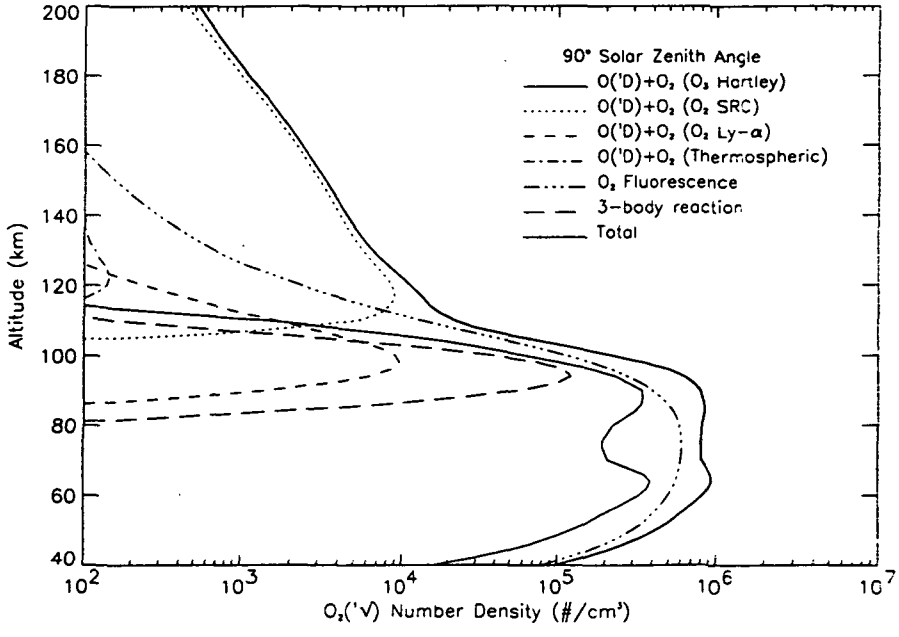

Figure 3. Calculated $O_2(^1\Sigma)$ number density profile at 90° solar zenith angle under the same geophysical conditions as Figure 2

Figure 4 presents the calculated $O_2(^1\Sigma)$ number density profiles under low and high solar activities. It is known that the solar spectral irradiance is modulated by solar activity, with its largest amplitude variation (> 1 order of magnitude) at ultraviolet and radio wavelengths (White, 1977). This variation has a profound impact on the heating and composition of the upper atmosphere and the ionosphere. The expansion of the atmosphere coupled with increasing ionization and excitation give rise to the larger $O_2(^1\Sigma)$ concentration found in the lower thermosphere above 120 km. In addition, the solar irradiances vary by approximately a factor of two at Lyman-α within the 11-year solar cycle and, although still questionable, by possibly ~20-50% near the SRC spectral region (Lean, 1991). This variation would result in the ~20-50% increase in $O_2(^1\Sigma)$ concentration near 100 km as indicated in Figure 4. Since there is very little variation in solar MUV (~0.1%) and visible (<0.08%) irradiances, the $O_2(^1\Sigma)$ concentration is insensitive to solar cycle variation below ~90 km. In other words, any possible variation one may observe in the $O_2(^1\Sigma)$ concentration or the subsequent emission rate near 60 km could only be due to the actual variation in the O_3 concentration. It should be noted that the O_3 concentration in the stratosphere and mesosphere will be perturbed due to a combination of effect resulting from changes in O_2 and O_3 photodissociation rates and changes in atmospheric temperature which affects temperature dependent chemical

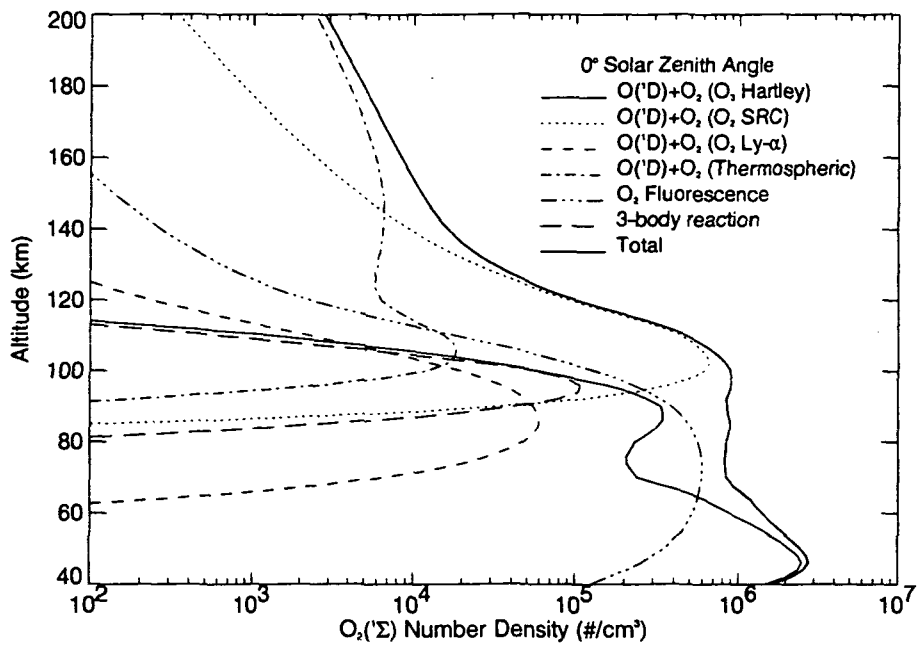

Figure 4. Calculated $O_2(^1\Sigma)$ number density profiles at 0° solar zenith angle under high and low solar activities.

reaction rates (Frederick, 1977; Allen et al., 1984; Eckman, 1986). These effects were not considered here in this investiation. However, it does suggest that the O_2 Atmospheric band emission can be used to monitor the O_2 and O_3 photolysis rates and the variation of O_3 concentration as a function of solar activity. This will be addressed in the later section when we discuss the remote sensing application of $O_2(^1\Sigma)$ dayglow emission.

2.2 O_2 Atmospheric Band Volume Emission Rates

The formula described previously calculate the total number density of $O_2(^1\Sigma)$ molecules in the daytime atmosphere. The volume emission rate of the total O_2 Atmospheric band system, η_{O2ATM}, is related to the density of $O_2(^1\Sigma)$ by

$$\eta_{O_2\,ATM} = A_{O_2(^1\Sigma)}[O_2(^1\Sigma)] \qquad (2)$$

where $A_{O2(1\Sigma)}$ is the Einstein transition probability of $O_2(^1\Sigma)$ to $O_2(^3\Sigma)$ state (~0.0833 sec^{-1}). In order to calculate the volume emission rates of any vibrational band in the system, $\eta_{\upsilon'\upsilon''}$, one needs to know the vibrational distribution of $O_2(^1\Sigma, \upsilon')$,

$$\eta_{\upsilon'\upsilon''} = A_{\upsilon'\upsilon''}[O_2(^1\Sigma,\upsilon')]. \quad (3)$$

Here $A_{\upsilon'\upsilon''}$ is the transition probability of $O_2(^1\Sigma,\upsilon')$ to $O_2(^3\Sigma,\upsilon'')$ state. Slanger (1986) has discussed the vibrational excitation processes for $O_2(^1\Sigma)$ molecules in aurorae and in the nightglow. In addition to the energy transfer reaction between $O(^1D)$ and O_2 (Lee and Slanger, 1978), the $\upsilon'= 0, 1$ of the $O_2(^1\Sigma)$ molecules in the daytime mesosphere and lower thermosphere can also be produced by the fluorescence excitation of $O_2(^3\Sigma,\upsilon''=0)$ at ~762nm and ~689nm (Bucholtz et al., 1987; DeMajistre and Yee, 1995). The laboratory results of Lee and Slanger (1978) showed that, in spite of the near resonance between $O(^1D)$ and $O_2(^1\Sigma,\upsilon'=2)$, only $\upsilon'= 0, 1$ of the $O_2(^1\Sigma)$ state are observed at 300 K with branching ratios β_o and β_1 of ~0.59 and ~0.41 respectively. The $O_2(^1\Sigma,\upsilon'=1)$ molecules are mainly quenched by ground state O_2 with a vibrational relaxation rate coefficient of 2.2×10^{-11} $cm^3 molecule^{-1} s^{-1}$ at 300 K. In a region where the collisions are frequent, the $O_2(^1\Sigma)$ molecules will most likely be in vibrational equilibrium and very small fraction is expected to be in $\upsilon'=1$ at the atmospheric temperature of ~200K. Consequently, the ratio between emission rates of O_2 (1-1) and (0-0) bands is very small at low altitudes. However, in the thermosphere where the collisions are less frequent, the vibrational distribution of the $O_2(^1\Sigma)$ molecules will retain signatures of how they are originally produced, giving rise to an $O_2(1,1)$ emission which does not follow the local thermodynamic equilibrium (LTE) predictions. The non-LTE vibrational distribution of $O_2(^1\Sigma,\upsilon')$ has been reported by previous dayglow observations of Skinner and Hays (1986) and Torr et al. (1986).

Since the vibrational quenching process of $O_2(^1\Sigma,\upsilon'=1)$ by O_2 is 151 cm^{-1} endothermic and has been found to be extremely rapid (2.2×10^{-11} $cm^3 molecule^{-1} s^{-1}$), the reaction is most likely to be an electronic energy-exchange reaction. In other words, considering electronic energy transfer collisions between $O_2(^1\Sigma,\upsilon')$ and ground state $O_2(^3\Sigma)$ molecules,

$$\begin{aligned} O_2(^1\Sigma,\upsilon'=1) + O_2(^3\Sigma,\upsilon''=0) &\xrightarrow{k_{10}} O_2(^1\Sigma,\upsilon'=0) + O_2(^3\Sigma,\upsilon''=1) \\ O_2(^1\Sigma,\upsilon'=0) + O_2(^3\Sigma,\upsilon''=1) &\xrightarrow{k_{01}} O_2(^1\Sigma,\upsilon'=1) + O_2(^3\Sigma,\upsilon''=0) \end{aligned} \quad (4)$$

one can relate the $O_2(^1\Sigma)$ $\upsilon'=0\rightarrow1$ energy-exchange rate coefficent k_{01} to the $1\rightarrow0$ energy-exchange rate coefficient k_{10} by

$$k_{01} = k_{10} \exp(-\Delta E/kT) \qquad (5)$$

through thermodynamic considerations of detailed balance, where k is Bolzmann's constant, T is the kinetic temperature, and ΔE is the endothermicity in the $1 \rightarrow 0$ vibrational relaxation reaction (-151 cm^{-1}). In fact, the reverse reaction ($\upsilon'=0 \rightarrow 1$) for the $\upsilon'=1$ production is 151 cm^{-1} exothermic and the rate coefficient k_{01} should be slightly more rapid than k_{10}. However, it requires a collisional partner of ground state O_2 at $\upsilon''=1$. As a result, at low temperature the net production rate of $O_2(^1\Sigma,\upsilon'=1)$ through the electronic energy-exchange reaction is still extremely small.

If the production rates of $O_2(^1\Sigma,\upsilon'=0)$ and $O_2(^1\Sigma,\upsilon'=1)$ by process k are denoted by $P_{0,k}$ and $P_{1,k}$, the steady-state concentrations of $O_2(^1\Sigma,\upsilon'=0)$, n_0, and $O_2(^1\Sigma,\upsilon'=1)$, n_1, can easily be calculated by solving the following matrix equation,

$$\begin{bmatrix} A_0 + k_{01} n_{O_2(\upsilon''=0)} + \sum_j k_{q,j} n_{X_j} & -k_{10} n_{O_2(\upsilon''=1)} \\ -k_{01} n_{O_2(\upsilon''=0)} & A_1 + k_{10} n_{O_2(\upsilon''=1)} + \sum_j k_{q,j} n_{X_j} \end{bmatrix} \begin{bmatrix} n_0 \\ n_1 \end{bmatrix} = \begin{bmatrix} \sum_k P_{0,k} \\ \sum_k P_{1,k} \end{bmatrix} \qquad (6)$$

where n_{X_j} are the number densities of electronic quencher X_j, k_q are the electronic quenching rate coefficients. A_0, A_1 are the total transition probabilities of $O_2(^1\Sigma,\upsilon'=0)$ and $O_2(^1\Sigma,\upsilon'=1)$ to the ground state $O_2(^3\Sigma)$ respectively and they are approximately equal to $A_{O_2(^1\Sigma)}$ of ~0.0833 sec^{-1}. $P_{0,k}$ and $P_{1,k}$ are the production rate of $O_2(^1\Sigma)$ by reaction k at $\upsilon'=0$ and $\upsilon'=1$ respectively.

Figure 5 shows the calculated number densities of $O_2(^1\Sigma)$ molecules at $\upsilon'=0$ and $\upsilon'=1$ as a function of altitude under the same geophysical conditions as Figure 2. The fluorescence excitation rate of $O_2(^1\Sigma)$ at $\upsilon'=0$ state and $\upsilon'=1$ state are calculated using the methods developed by DeMajistre and Yee (1994). The three-body recombination process may have enough energy to produce vibrationally excited $O_2(^1\Sigma)$ molecules. However, due to lack of information on the exact kinetics of the O_2 states involved, we have assumed that all the $O_2(^1\Sigma)$ molecules produced are in the $\upsilon'=0$ state. Since it is a minor source and only occurs in the region near 95 km where the vibrational quenching still dominant, this assumption has very little impact on the final steady-state number density of the $O_2(^1\Sigma)$ at $\upsilon'=0$. In addition, there is no laboratory measurement on how the electronic quenching reaction varies with vibrational state of $O_2(^1\Sigma)$. We therefore have assumed that the electronic quenching rates are independent of $O_2(^1\Sigma)$ vibrational levels.

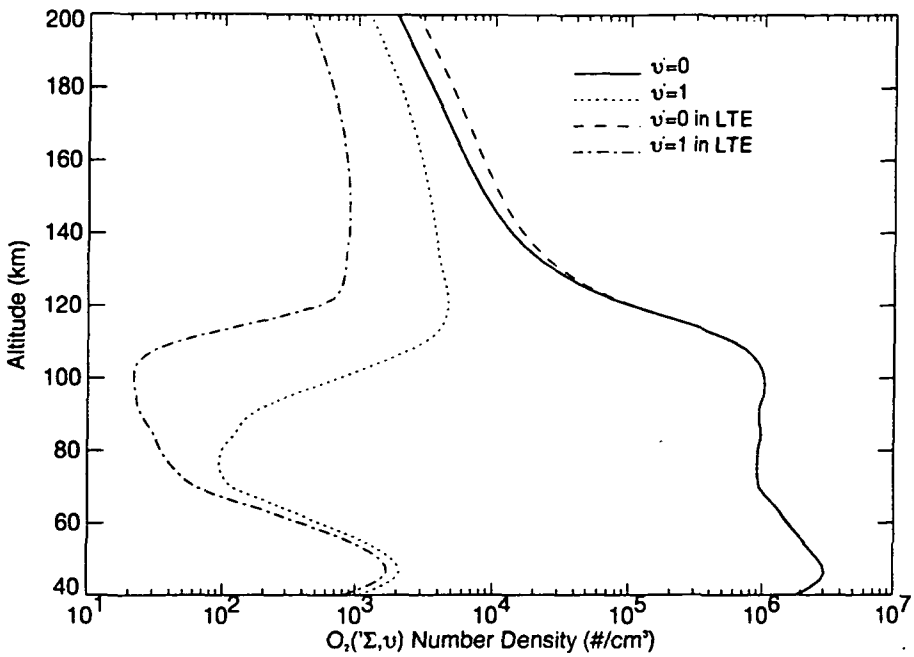

Figure 5 Calculated $O_2(^1\Sigma)$ number density for vibrational levels υ'=0 and 1 under the similar geophysical condition in Figure 1.

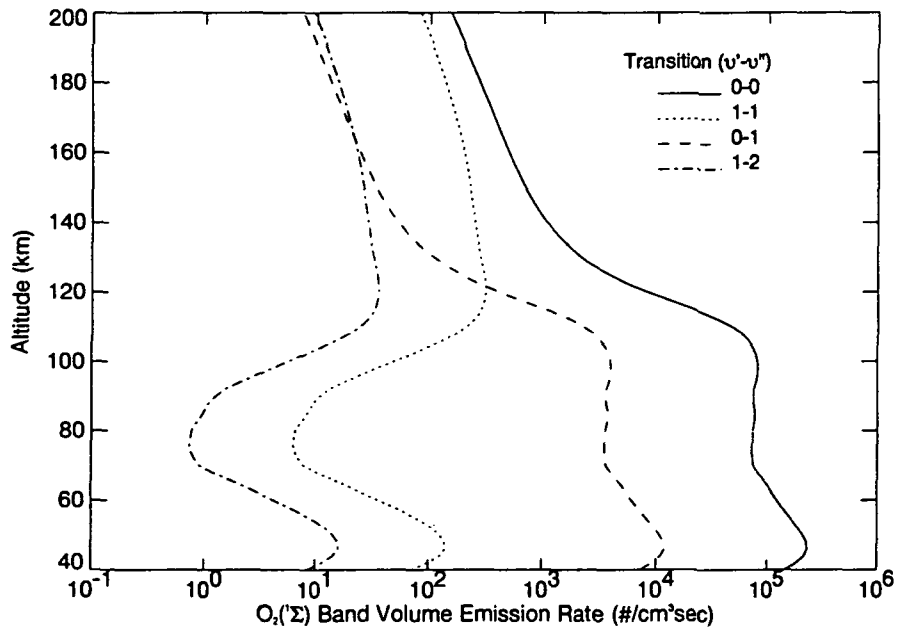

Figure 6. Calculated O_2 (0-0),(0-1),(1-1),and (1-2) Atmospheric band volume emission rate profiles under the similar geophysical condition in Figure 1.

As indicated in Figure 5, the $O_2(^1\Sigma)$ molecules are very close to vibrational equilibrium below ~70 km and deviate from the Bolzmann distribution above ~150 km with a significant larger $\upsilon'=1$ population than the value under LTE condition. Figure 6 shows the calculated volume emission rate profiles of O_2 Atmospheric (0,0), (0,1), (1,1), (1,2) band emissions. At altitudes above 160 km where vibrational relaxation is not important, the emission rate ratio between (0,0) and (1,1) bands is a constant value of ~1.4, given by the $\beta_o * A_{0\text{-}0}/\beta_1 * A_{1\text{-}1}$ where β_o and β_1 are the branching ratios of the initial production, $A_{0\text{-}0}$ and $A_{1\text{-}1}$ are the Einstein transition probabilities of O_2(0-0) and (1-1) bands respectively.

Figure 7 shows the calculated (0-0) band volume emission rate profile under similar geophysical conditions (i.e. F10.7= , SZA=75.5, Ap= xx) during the rocket experiments reported by Wallace and Hunten (1968). Our theoretically calculated emission rates compare reasonably well with the observed values and the small disagreement found here is most likely due to the difference in the actual composition profiles used in our model.

2.3 Spectral Limb Brightness

In general the quantity that any optical instruments measure from the ground or from space is the line-of-sight brightness of the spectral feature of interest. The measured spectral brightness from a spaceborne instrumentation is an integrated volume emission rate along the slant path associated with a particular tangent ray altitude. When the absorption is important, such as the O_2 Atmospheric (0-0) band, the measured brightness is modified by the attenuation along the path between the emitting region and the spacecraft.

If we denote the volume emission rate of any $O_2(^1\Sigma,\upsilon'\text{->}\upsilon'')$ emission band at a point along the line of sight by $\eta(s)$ (in photons/cm^3/sec) and the atmospheric volume scattering rate by $\eta_c(s)$ per wavenumber (in photons/cm^3/sec/cm^{-1}), the observed spectral brightness of one of its rotational line at ν_i as a function of wavenumber ν and tangent height z_t $B(\nu-\nu_i,z_t)$, is given by

$$B(\nu-\nu_i,z_t) = \int_{-\infty}^{\infty} [\eta(s) f_i(s) D(\nu-\nu_i,s) + \eta_c(s)] \exp\left\{-\int_s^{\infty} n(s')\sigma g_i(s') D(\nu-\nu_i,s')ds\right\} ds \quad (7)$$

where $f_i(s)$ and $g_i(s)$ are the relative line strengths of the rotation line of interest for emission and absorption respectively, and $\Sigma f_i = 1$ and $\Sigma g_i = 1$. n(s') is the number density of $O_2(X^3\Sigma_g^-,\upsilon'')$, and σ is the band absorption cross-section from υ'' to υ' (xxxx , 19xx). $f_i(s)$ and $g_i(s)$ are determined by the rotational temperatures T(s) of $O_2(b^1\Sigma_g^+,\upsilon')$ and $O_2(X^3\Sigma_g^-,\upsilon'')$,

$$f_i(s) = f_{s,i}\frac{T_s}{T(s)}\exp\left\{\frac{1.439\,E'(T(s)-T_s)}{T(s)T_s}\right\},$$
$$g_i(s) = g_{s,i}\frac{T_s}{T(s)}\exp\left\{\frac{1.439\,E''(T(s)-T_s)}{T(s)T_s}\right\}. \qquad (8)$$

Here $f_{s,i}$ and $g_{s,i}$ are the relative line strengths at standard temperature T_s, and E' and E'' are the energies in cm^{-1} for the rotational line i of the excited state $O_2(b^1\Sigma_g^+,\upsilon')$ and ground state $O_2(X^3\Sigma_g^-,\upsilon'')$ respectively (Babcock and Herzberg, 1948). $D(\nu-\nu_i,s)$ is the emission or the absorption line shape at position s and shifted by the component of the atmospheric wind along the line of sight. In the region above 40 km where the pressure broadening is not very important, the spectral line shapes are determined by the kinetic temperatures of the excited state $O_2(b^1\Sigma_g^+)$ (for emission) and the ground state $O_2(X^3\Sigma_g^-)$ (for absorption) respectively,

$$D(\nu-\nu_i,s) = \frac{1}{\alpha_D(s)}\left[\frac{\ln 2}{\pi}\right]^{\frac{1}{2}}\exp\left\{\frac{\left(\nu-\nu_i-\frac{v(s)}{c}\right)^2\ln 2}{\alpha_D^{\,2}}\right\} \qquad (9)$$

where c is the speed of light, v(s) is component of the atmospheric wind velocity along the line-of-sight, and α_D is the doppler width,

$$\alpha_D(s) = \frac{\nu_i}{c}\left[\frac{2kT(s)\ln 2}{m}\right]^{\frac{1}{2}} \qquad (10)$$

Here, k is the Boltmann constant, and m is the molecular mass of O_2.

Converting the line-of-sight integral in Eq.(5) to an integral in altitude z, one obtains

$$B(\nu - \nu_i, z_t) = \int_{z_t}^{\infty} [\eta(z) f_i(z) D(\nu - \nu_i, z) + \eta_c(z)] W(z, z_t) \exp\{-\Gamma(\nu - \nu_i, z, z_t)\} dz$$
$$+ \int_{z_t}^{\infty} [\eta(z) f_i(z) D(\nu - \nu_i, z) + \eta_c(z)] W(z, z_t) \exp\{-\Gamma(\nu - \nu_i, z_t, z_t) - \tau(\nu - \nu_i, z, z_t)\} dz \quad (11)$$

where $W(z,z_t)$ is the Jacobian in the transformation ($W = \_s/\_z$), or the geometric weighting function,

$$W(z, z_t) = \frac{R_e + z}{\sqrt{(R_e + z)^2 - (R_e + z_t)^2}} \quad (12)$$

R_e is earth radius, and

$$\Gamma(\nu - \nu_i, z, z_t) = \int_{z}^{\infty} n(z') \sigma g_i(z') D(\nu - \nu_i, z') W(z', z_t) dz', \quad (13)$$

$$\tau(\nu - \nu_i, z, z_t) = \int_{z_t}^{z} n(z') \sigma g_i(z') D(\nu - \nu_i, z') W(z', z_t) dz'. \quad (14)$$

Since

$$\Gamma(\nu - \nu_i, z, z_t) = \Gamma(\nu - \nu_i, z_t, z_t) - \tau(\nu - \nu_i, z, z_t) \quad (15)$$

and let

$$\Gamma(\nu - \nu_i, z_t) = \Gamma(\nu - \nu_i, z_t, z_t), \quad (16)$$

Eq(8) becomes

$$B(\nu - \nu_i, z_t) = \int_{z_t}^{\infty} 2[\eta(z) f_i(z) D(\nu - \nu_i, z) + \eta_c(z)] W(z, z_t)$$
$$\exp\{-\Gamma(\nu - \nu_i, z_t)\} \cosh\{\tau(\nu - \nu_i, z, z_t)\} dz \quad (17)$$

The above equation computes the spectral brightness, $B(\nu - \nu_i, z_t)$, of any given rotational line when the self-absorption process is considered. The spectral brightness in this case not only depends upon the band volume emission rate and the O_2 number density profiles, but also on the atmospheric temperature and wind profiles. For emissions that the self-

absorption process is not important, such as the O_2 Atmospheric (0-1) and (1-1) bands, Eq.(14) becomes the Abel integral equation (Hays et al., 1973),

$$B(\nu - \nu_i, z_t) = 2\int_{z_t}^{\infty} [\eta(z) f_i(z) D(\nu - \nu_i, z) + \eta_c(z)] W(z, z_t) dz, \qquad (18)$$

and the spectral brightness is determined by the total band volume emission rate and the atmospheric temperature profiles.

Figure 8 shows the calculated spectral brightness of a relatively strong line (RQ5 at 13138.192 cm^{-1}) of O_2(0-0) band at tangent height 60 km assuming there is no doppler shift (atmospheric wind and spacecraft velocity induced shift). The spectral line shape for neglecting the self-absorption is also shown for comparison. Since the magnitude of the absorption cross-section is the largest at the line center and decreases toward the wings, the effect of the self-absorption process gives rise to a broadened emission line shape and an effective temperature larger than the kinetic temperature of the emitters.

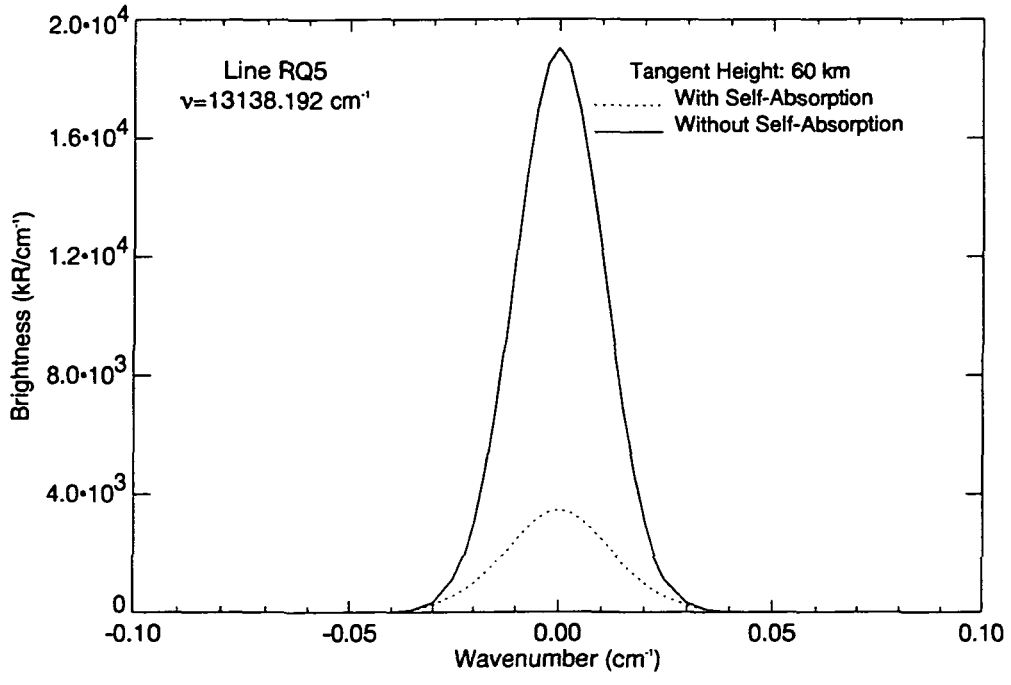

Figure 8 Calculated spectral line brightness with and without the effect of self-absorption for RQ5 of the O_2(0-0) band as observed at tangent height of 60 km

Figure 8 presents the calculated band spectra of O_2 Atmospheric band system near 760nm *at tangent heights of* (a) 60 km and (b) 150 km respectively.

It should be noted that, in principle, the accurate calculation of $B(\nu-\nu_o,z_t)$ is extremely computational extensive due to the magnitude of doppler shift ($\sim<10^{-5}$ cm^{-1}) as compared to the width of the line. For any practical use of the above equations, such as deriving inversion kernels for atmospheric remote sensing, one needs to use computationally efficient and reasonably accurate expressions. These approximated equations will be presented in our subsequent papers when the inversion algorithm and equations are introduced.

3. MEASUREMENTS OF O_2 ATMOSPHERIC BAND DAYGLOW EMISSIONS

In this section, we will describe in details how the $O_2(^1\Sigma)$ molecules are excited in the terrestrial atmosphere and how the spectral band brightness and the spectral line shape of any individual rotational line are affected by the atmospheric O_2 number density, wind, and tempeature profiles. We will compare our model results with some existing experimental dayglow data obtained under various geophysical conditions in the previous rocket and satellite experiments (i.e. solar activities, solar zenith angle, etc.).

The experimental data, as summarized in Table 2.1, include the rocket measurements of Wallace and Hunten (1968), broadband FPI/DE measurements of Skinner and Hays (1985), the high resolution line shape measurements of HRDI/UARS, and medium resolution spectral brightness measurements obtained during our recent rocket experiments. Two sets of rocket campaign data, conducted from White Sands, New Mexico during the summer of 1989 and Poker Flat, Alaska during the winter of 1994, will be used in our study. We will study the $O_2(^1\Sigma)$ photochemistry, its solar zenith angle variation, and the vibrational distribution of $O_2(^1\Sigma,\upsilon')$ molecules by comparing with measured band volume emission rate profiles. We will also examine the effect of self-absorption on the spectral line shapes and the total (0-0) and (0-1) band brightness as a function of tangent height.

Table 2.1 Summary of the previous measurements used in the current study

	Experiment 1	**Experiment 2**	**Experiment 3**	**Experiment 4**	**Experiment 5**

Observational Platform	Rocket (KP3.16)	Satellite (DE)	Satellite (UARS)	Rocket (NASA 27.122)	Rocket (NASA 27.122)
Reference	Wallace and Huntem(1976)	Skinner and Hays (1984)	Hays et al. (1993)	See Text	See Text
Instruments	Photometer	FPI	FPI	Spectrograph	Spectrogragh
Features	Spectrum	Spectrum	Emission lines	Spectrum	Spectrum
Measurements	(0-0) and background	(0-0) and (1,1)	(0-0)	(0-0),(1-1) and (0-1), (1-2)	(0-0),(1-1) and (0-1), (1-2)
Date(s)	Oct.11, 1966		1992-present	July 27, 1989	Feb. 1, 1993
Time	16:22 MST			10:00 LT	12:00 LT
Location	Poker Flat			White Sands	Poker Flat
SZA (degree)	75.5			~10.0	81.0
F10.7 cm					
Ap					

In this section, we will describe in details how the $O_2(^1\Sigma)$ molecules are excited in the terrestrial atmosphere and how the spectral band brightness and the spectral line shape of any individual rotational line are affected by the atmospheric O_2 number density, wind, and tempeature profiles. The model presented in this section will be used to examine the line shape measurements taken by the HRDI instrument onboard UARS and spectral brightness measurements taken by the DATES instrument during several rocket experiments.

2.1.1 Density and Temperature Spectrograph (DATES)

DATES instrument is one of the suite of instruments onboard the NASA Michigan Airglow Package (MAP) rocket experiment designed to study the photochemistry of ozone in the daytime mesosphere and lower thermosphere. The DATES experiments involve the measurements of dayglow emission spectra in two important O_2 Atmospheric band spectral regions: (1) near 760 nm for the (0-0) and (1-1) bands, and (2) near 860 nm for the (0-1) and (1-2) bands. The primary objective of DATES is to provide accurate measurements of the atmospheric O_2 density and temperature from the spectral characteristics of the measured O_2 Atmospheric band emissions.

The basic component of DATES, as illustrated in Figure 3.1, consists of a baffled telescope, a 1/4 meter Ebert spectrometer, and a Charge-Couple-Device (CCD) detector. The optical characteristics of DATES instrument are determined by the desire to view the Earth's limb with 2 km vertical resolution and to perform the measurements (750 nm to 880nm) in a reasonable time period (i.e. long enough to achieve the desired measurement accuracy and short enough to avoid spatial smearing). These desires are further constrained by the need to baffle the instrument against brighter signal coming from lower tangent heights. DATES employs a thermo-electrically frame-transfer Thompson TH7882 CCD (576x384 pixels) as its detector. The CCD is used for its high quantum efficiency (beyond 850 nm), linear response, and large dynamic range. The area-array CCD format allows an emission spectrum to be collected without mechanically moving the grating with a spectral coverage determined by the grating dispersion and the physical dimension of the CCD chip. A 1200 lines/mm holographic grating was used in NASA 27.122 rocket experiment (# 4 in Table 2.1), giving a simultaneous spectral coverage of ~230Å. During the follow-on NASA 27.133 campaign (#5 in Table 2.1), the lower density grating was used to increase the spectral coverage to ~460Å.

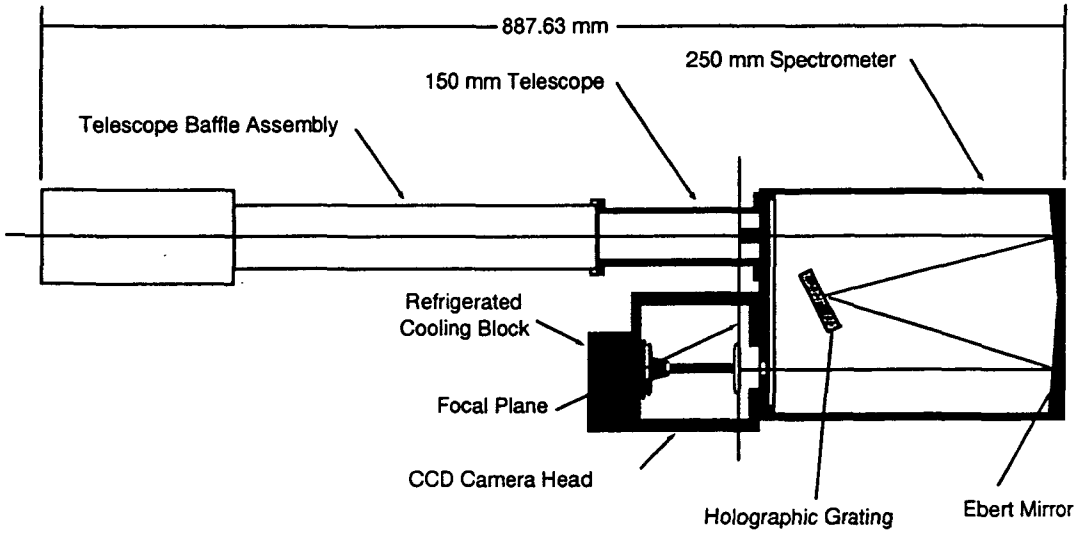

Figure 2.1 DATES Schematics drawing

Optics: DATES has a field of view of 0.0717 x 2.52 degrees defined by an objective lens with focal length of 150 mm and an input slit of 0.1877 x 6.62 mm. The optical design was fully raytraced and carefully optimized to minimize the off-axis blurring due to optical aberration.

Telescope and Baffle: DATES observes the atmosphere on its limb through a two-stage baffled f-5 telescope. The telescope provides the light collection and pointing, and directly feeds the light collected to the spectrometer. The baffle is similar in design to the ones used in the Visible Airglow Experiment (VAE) photometers on the Atmosphere Explorer Satellites and the Fabry-Perot Interferometer (FPI) on the Dynamic Explorer Satellite. The purpose of the baffle system is to eliminate stray light which enters the optics from the bright limb of the Earth from lower tangent height. Internal baffles are also installed within the spectrometer to further minimize the scattering light.

Ebert-Fastie Spectrometer: DATES uses a 1/4 meter Ebert mirror and a 1200 lines/mm (later changed to 600 lines/mm) holographic grating. It operates on the first interference order for the measurements of (0-0) 7620Å and (0-1) 8600Å spectral regions. A blocking filter which eliminates the photons with wavelength shorter than 6000Å is installed to prevent the photons of higher order dispersion from reaching the detector. The spectrometer is preset at two grating angles controlled by a solenoid switch so that two spectral regions can be measured alternatively.

CCD Detector: The grating-dispersed spectrum is imaged onto a frame transfer area-array CCD detector and detection of the spectra is accomplished by using a CCD with on-chip binning to determine the spectrum of interest. The DATES CCD detector system is a modified Photometric CCD camera head with a Thompson TH7882 frame transfer CCD chip installed within it. The CCD chip is cooled using a three-stage thermoelectric cooler with flowing liquid coolant in order to decrease the thermal noise. The coolant temperature is maintained by a pump, a pre-frozen ice bucket, and a thermal radiator. During operation of the rocket flight, the sink temperature was maintained at 0 degree C, giving the CCD temperature of approximately -36.5 degree C. The dark current at this temperature was measured to be ~14 electrons per pixel per second.

DATES Control Electronics: The DATES electronic package consists of three main sections: CCD electronic card stack, control computer stack, and power supply modules. All phases of instrument operation are under the direct control and supervision of the DATES control computer. The CCD card stack contains all the electronics required to control the vertical and horizontal shifting (binning) of the CCD pixel registers, power control of the CCD thermal electric cooler and regulating heater, a low noise double correlation A/D conversion of the CCD data (~15.6 electrons per digital count), and a command receiver which puts all functions under the control of an external controller.

The DATES control computer stack consists of a processor board based upon an Intel 16 bit 8096 microcontroller, a command board that sends commands to the CCD card stack, a telemetry board which interfaces with the rocket telemetry system, and a calibration lamp and thermoelectric cooler (TEC) controller for closed loop control of the TEC.

The power supply modules consist of two Dale DC-DC converters that provide the +5 V and the +/- 15 V required by the system.

DATES Operations: All phases of instrument operation were under the direct control and supervision of the DATES control computer. The control computer contains a nonvolatile memory which helds up to 8 different operating modes, 7 of which could be programmed to change such things as grating position (i.e. one of the two spectral modes) CCD readout binning pattern, and integration time, etc. A sequence of operating modes were then conducted basing upon time marks determined from the pre-flight attitude and pointing information. For both flights it started with ~60 seconds of instrument calibration before the nose cone came off in order to monitor the stability of the instrument (i.e. the sensitivity and instrument wavelength drift). At ~60 seconds after launch, DATES was switched to pre-programmed science modes. These modes include the measurements of the O_2 Atmospheric (0-0) and (0-1) band emissions (two pre-set grating angles) with various CCD binning patterns at a constant CCD readout period of 0.25 second. The number of CCD readouts for each spectral observation before grating angle changes varied from 8 (2 minutes) for the NASA 27.122 flight to 12 (3 minutes) for the 27.133 flight. Since the (0-0) band emission was ~20 times stronger than that of the (0-1) band, only part of the CCD spatial pixels (1/8 of the frame for the 27.122 flight and 1/3 frame for the 27.133 flight) were read to avoid CCD pixel full-well saturation and 14-bit digital readout maximum (16383). During the ascending leg of the 27.133 campaign before the rocket axis tilted to start the limb observations, DATES only measures the spectral brightness of the (0-0) band under a CCD binning pattern which gives the highest sensitivity (full frame 288 pixels summing mode). A summary of DATES instrumental parameters for the two rocket experiments are given in Table 2.2.

Table 2.2. Summary of DATES Instrument Parameters

	NASA 27.122	NASA 27.133
Field-of-view	0.0717° x 1.26°	0.0717° x 1.26°
Input Slit Size	0.38 x 6.62 mm	0.38 x 6.62 mm
Grating Density	1200 lines/mm	600 lines/mm
Spectral Coverage	(0-0): ~234 Å, (0-1): ~222 Å	(0-0): ~234 Å, (0-1): ~222 Å
Resolution	13.4 Å	

CCD Binning Pattern	(0-1): 12x288 (zenith) 12x288 (limb) (0-0): 12x36 (zenith) 12x36 (limb)	(0-1): 3x288 (limb) (0-0): 3x288 (zenith) 3x96 (limb)
Spectral Channels	32	128
Sensitivity (elec/sec/R/Å)	1.2 @7600 Å 0.8 @8600 Å	1.2 @7600 Å 0.8 @8600 Å
CCD Readout Period	0.25 second	0.25 second
Mode duration	2 minutes (8 frames)	3 minutes (12 frames)

Sources of Measurement Uncertainty: The accuracy of any measurement is governed by the accuracy of the instrument calibration and the counting statistics. In addition to the photon statistics (which usually follows the Poisson distribution), there exist many sources of error concerning the output CCD digital counts. The DATES TH7882 CCD chip, in general, is well-behaved, and the preamplifier output has a very low noise (less than ten electrons at 30 kHz). The combined preamplifier noise and the bias noise for the DATES CCD detector system are found to be ~30 electrons or 2 counts per read. This is negligibly small compared to the dark current, which runs at appproximately 775 counts (~12,096 electrons) per 0.25 second after the pixel binning (12 by 288 pixels) at -36.5° C.

The dark current of the CCD detector, like the photon statistics, is also found to follow the Poisson distribution. In other words, for a single measurement of dark signal of 775 counts (or 12,096 electrons), the uncertainty is $\sim(12{,}096)^{1/2}$ electrons or 7.05 counts, a mere <1% uncertainty. For the magnitude of signals (~1000 digital counts per 0.25 second) that DATES observed (shown in the next section), the statistical uncertainty is less than a fraction of one percent.

2.1.2 Observation: NASA 27.122 campaign

All DATES experiments have been carried out in conjunction with the NASA MAP rocket campaigns and launched by Nike Black sounding rockets. During the 27.122 campaign, the solar zenith angle was ~10 degree at the time of the launch, and the payload reached an apogee of 223 km about 245 seconds into the flight. An inertial attitude control system (ACS) oriented the spectrograph for viewing the north-eastern horizon. The limb observation commenced at a rocket altitude of ~190 km (~160 seconds into the flight) when the DATES line of sight had been positioned at 10.9° below the local horizon at a solar azimuthal angle of 87.7°. A solar azimuth angle of close to

90° during local noon made the scattering angle near 90°, consequently minimizing the continuum scattered light. This orientation was maintained until the rocket reached at an altitude of 210 km (~190 seconds) where the rocket spin axis (DATES optical axis) was pitched up at a rate of 0.184°/second to view the lower thermosphere at ~3.5 km/second. At the apogee (~245 seconds), the spectrograph was pitched back down at the same rate during the descent until ~300 seconds or the rocket descended down to ~205 km to repeat the observations of the lower thermosphere. After 300 seconds the rocket orientation was maintained again at 10.9° below the horizontal which let the descent of the rocket do the tangent height scan which rans at ~1 km/second. While the rocket orientation was maintained at 10.9° below the horizontal during both the ascend and descent legs of the flights (~ 40 to 50 seconds), the spectrograph was able to measure the spectral brightnesses of the (0-0) and (0-1) emission bands between tangent altitudes of 50 and 105 km.

Figure xx(a) and (b) present the measured (0-1) and (0-0) band emission spectra as a function of flight time taken during the 27.122 campaign. The DATES operational modes during this flight were designed to alternately measure the O_2(0-0) and O_2(0-1) band spectral brightness in 32 spectral channels. Each spectral band was observed for 2 seconds during which eight spectra were collected (CCD readout time of 0.25 second) before changing to the other band. Among these eight spectra, the first one was always discarded due to contamination from the movement of the grating during exposure. According to the rocket attitude data, a tangent height of 70 km is observed at ~160 seconds after launch during the upleg and a tangent height of 60 km at ~360 seconds after launch during the downleg. The time range from T+160 seconds to T+195, and T+300 to T+360 seconds gives an upleg tangent height scan from 65 km to about 110 km, and downleg scan from 110 km to 53 km. The O_2 P (> 762 nm) and R (< 762 nm) branch spectral features were clearly observed with very little noise. During this flight, two thermospheric scans were also obtained between T+195 and T+270 seconds. The spectral features, however, were relatively weak and consequenlty, they were not revealed in this figure due to the linear scale.

The spectral signals for both (0-1) and (0-0) band emissions as a function of tangent height between 60 and 120 km are shown in Figure xx. The increasing continuum signals with decreasing tangent height due to Rayleigh scattering were clearly observed in both of the (0-1) and (0-0) band spectral observations. In contrast, the O_2(0-0) band emission superimposed on the contiuum is significantly different from the (0-1) band emission. The (0-0) band brightness becomes weaker as the tangent height, while the (0-1) band

brightness increases with decreasing tangent height. This is due to the self-absorption effect that we will discuss in details later in the next section. Although not very clear in these figures, the small enhancements in signal near 770 nm and 870 nm for tangent heights above 100 km correspond to those of the O_2(1-1) and (1-2) band emissions respectively. These two emissions, originating from the vibrationally excited $O_2(^1\Sigma,\upsilon'=1)$ molecules, become relatively more important as the tangent height increases. In fact, some emissions from the N_2 first positive system (N_2 $B^3\Pi_g$ -> $A^1\Sigma_g$) also contribute to the observed (0-0) and (0-1) band spectra. Figure xx(a) shows the measured (0-1) band spectra at a tangent height of 90 km. We found that the observed spectra is dominated by the O_2(0-1) band emission with small contributions from the O_2 (1-2) band and N_2 1st Positive (1-0) and (2-1) band emissions. A rotational temperature of 500 K has been assumed for the N_2 1PG system since its emission originates in the lower thermosphere near 150 km. Rotational temperature of ~210 K and 601 K are obtained from the fit for the O_2 (0-1) and (1-2) bands, respectively. A higher rotational temperature for the (1-2) band suggests that its emission is mainly produced at an altitude higher than the (0-1) band. Other fitted parameters, such as band brightness, are also shown. The quality of the fit can be clearly demonstrated by looking at the comparison between the fitted and observed signals at the weaker emission channels, as shown in Fig. 25(b).

Figure 27(a) gives the measured (0-0) band spectra at a tangent height of 119 km. Excellent fit can be obtained, especially near the wings of the O_2(0-0) band emission as it is revealed in Fig. 27(b), if we include contributions from the O_2(1-1) and N_2 1st positive (3-1) and (2-0) band emissions. A rotational temperature of ~405 K is obtained for the (0-0) band emissions. At lower tangent height measurements, one has to consider self-absorption by O_2 in order to obtain a good fit to the observed spectra.

Figure 9 shows the brightnesses of O_2(0-0) and (1-1) bands as a function of tangent height.as observed by DATES spectrogragh onboard MAP rocket launched from White Sands on July 26, 1989. The characteristics of the spectrograph and the techniques used to obtain the band brightnesses presented here will be described in detail in a later paper (Yee et al., 1995). Our calculated band brightnesses under the same geophysical condition (i.e. SZA= , F10.7= , Ap=) agree with the measurements very well. The slight differences found at high altitudes are most likely due to the uncertainty in our modeling of daytime thermospheric $O(^1D)$ number density.

Figure 9 presents the calculated (0-0)/(0-1) ratio as a function of tangent height as compared to those observed by DATES rocket experiment and FPI/DE observations (Skinner, 1984). The remarkable agreement, especially at high tangent heights, between

model results and the observations suggests that the kinetic coefficents used in our vibrational relaxation model are reasonably sound.

This included the zenith observations taken when the instrument optical axis is pointing nearly vertical during the ascend, and the limb observations after the rocket axis tilted below the horizon ~150 seconds into the flight.
Figure

3. APPLICATION TO ATMOSPHERIC REMOTE SENSING

The measurement of $O_2(^1\Sigma)$ dayglow can provide some of the fundamental information concerning the basic states (pressure, wind, density and temperature) of the upper atmosphere and external energy input. These parameters can be recovered either from the spectroscopic properties of the $O_2(^1\Sigma)$ airglow emissions near ~760 nm (0-0 band) and ~890 nm (0-1 band) or from the photochemistry of the $O_2(^1\Sigma)$ molecules.

3.1 Atmospheric Temperature

The measured brightness of an emission line is an integrated volume emission rate along the slant path associated with a particular tangent ray altitude. The spectral brightness of any given rotational line of the observed O_2 Atmospheric band emissions depends on the atmospheric temperature profile in two different ways. One is the thermal distribution of the rotational levels of both the emitter, the excited $O_2(b^1\Sigma_g^+)$ and the absorber, the ground state $O_2(X^3\Sigma_g^-)$. The other temperature dependence arises when the spectral line shapes of the emission and the absorption cross-section are considered.

In a region where the self-absorption is not important, the doppler width of any line in the O_2 Atmospheric band system and its rotational band structure (i.e. 0-1 band above ~40 km and 0-0 band above 100 km) can yield a direct measurement of the thermodynamic state of the excited $O_2(^1\Sigma)$ molecule. The $O_2(^1\Sigma)$ molecules are mainly produced by processes with excess energy which may appear not only as kinetic energy but also vibrational and rotational excitations. The technique of recovering atmospheric temperature from spectroscopic measurements of this emission band thus depends on how close the $O_2(^1\Sigma)$ molecules are in thermodynamic equilibrium (i.e. the velocity distribution as well as rotational distribution). This, in turn, depends on the degree of

non-thermal distribution when the $O_2(^1\Sigma)$ molecules are initially produced and the number of collisions within their effective lifetime (before they are quenched or radiate).

The lifetime of a newly produced $O_2(^1\Sigma)$ molecule is inversely proportional to its loss rate, i.e. combination of spontaneous radiation and electronic (and vibrational if vibrationally excited) quenching collisions with N_2 and O_2. Figure 10 shows the typical lifetime of $O_2(^1\Sigma)$ molecules for $\upsilon'=0$ and $\upsilon'=1$ as a function of altitude. At altitudes below ~80 km where electronic quenching loss dominates over radiation, the lifetime of $O_2(^1\Sigma, \upsilon'=0)$ molecule decreases nearly exponentially with descreasing altitude. However, since the collision frequency is proportional to the ambient density (the same for the electronic quencher), the number of collisions of $O_2(^1\Sigma, \upsilon'=0)$ molecule within its lifetime remains at ~10^5 (based on a hard-sphere collision cross-section of 2×10^{-15} cm^2). As the effect of quenching diminishes above ~100 km with the radiation being the only loss mechanism, the lifetime is determined by its radiative lifetime of ~12 seconds. As a result, the number of collisions within its lifetime decreases exponentially with altitude, from ~2×10^4 at 100 km to ~70 at 200 km. In other words, in the region below 200 km, the newly created $O_2(^1\Sigma, \upsilon'=0)$ molecule will suffer at least ~70 collisions before it radiates or is quenched. Although the $O_2(^1\Sigma, \upsilon'=0)$ molecule can be produced with excess kinetic energy up to ~0.4 eV (the maximum exothermicity of the $O(^1D)+O_2$ reaction), translationally it will most likely be in local thermodynamic equilibrium (LTE) with the ambient atmosphere after suffering 70 collisions. The doppler temperature measured from the spectral line shape of any subsequent emissions (i.e. (0-0) band at 762 nm and (0-1) band at 865 nm) thus represent the true ambient kinetic temperature. As described in the previous section, the vibrational excited $O_2(^1\Sigma)$ molecule loses its vibrational energy very efficiently by colliding with ground state $O_2(^3\Sigma, \upsilon''=0)$. In fact, the vibrational quenching rate is approximately 4 order of magnitude more efficient than the electronic quenching (2.2×10^{-11} with O_2 versus 2.1×10^{-15} with N_2). The effective vibrational quenching of $O_2(^1\Sigma, \upsilon'=1)$ molecule by electronic energy transfer collisions with reduces the lifetime of $O_2(^1\Sigma, \upsilon'=1)$ molecules by 4 order of magnitude at altitudes below 80 km. It has been demonstrated that at high altitudes the vibrational distribution of $O_2(^1\Sigma)$ molecules is not in thermodynamic equilibrium. For collisional relaxation of excited $O_2(^1\Sigma)$ molecules, $kT/\Delta E$, is ~99 for rotational-translational (R-T) collisions (ΔE = ~1.4 cm^{-1}) as compared to ~0.097 for vibrational-translational (V-T) collisions (ΔE = ~1432 cm^{-1}) at a temperature of 200 K. Consequently, the R-T energy transfer is significantly more efficient than the V-T transfer rate and the $O_2(^1\Sigma)$ molecules are more likely to be in rotationally thermodynamic equilibrium. Below 150 km, the newly

produced $O_2(^1\Sigma)$ molecules are expected to suffer at least ~xxx collisions before they radiate. Without detailed thermodynamic calculation, it can be expected that the $O_2(^1\Sigma)$ molecules are very close to be in kinetically and rotationally thermodynamic equilibrium.

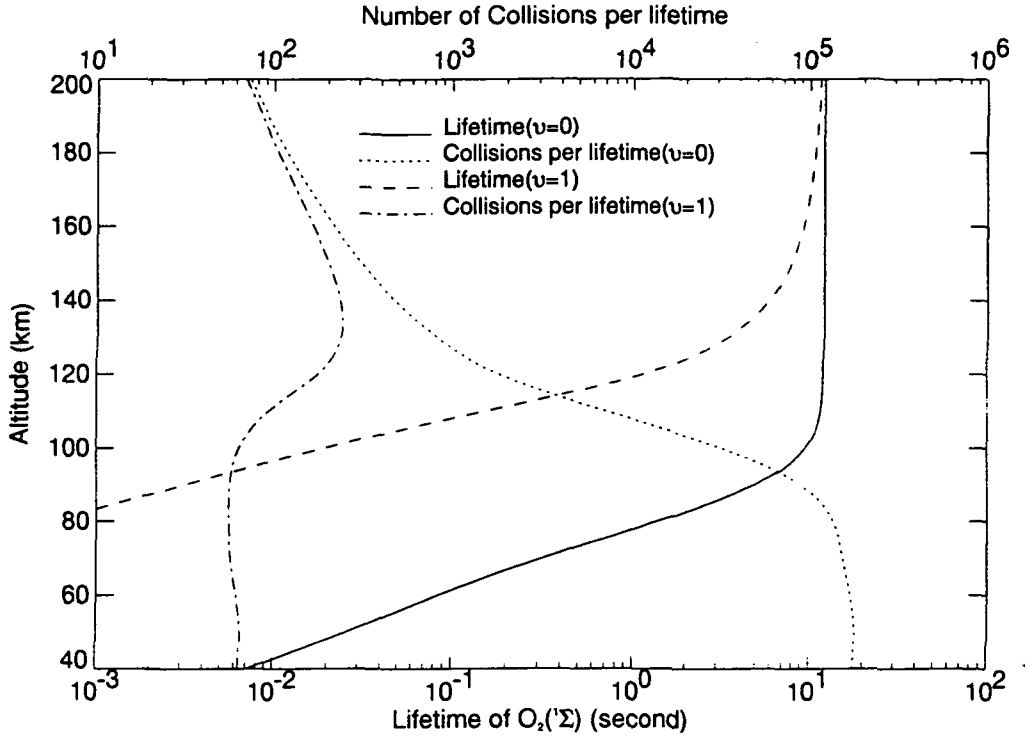

Figure xx. Lifetime of $O_2(^1\Sigma)$ molecule as a function of altitude and the number of collision with the ambient atmosphere within its lifetime

HRDI/UARS measures high resolution line spectra of three rotational lines of different line strengths in the O_2(0-0) band between 55 and 110 km. The doppler and rotational temperatures obtained should represent the ambient atmospheric kinetic temperature. However, one needs to consider the effect of self-absorption for these lines at some altitudes in order to properly retrieve the temperature information.

3.2 Atmospheric Density and Pressure

The optical thickness of an emission feature depends on the magnitude of the absorption cross-section and the column density of the absorber along the line-of-sight path. The O_2 Atmospheric (0-1) band is optically thin down to 40 km because the absorber $O_2(X^3\Sigma, \upsilon''=1)$ population is relatively low. For the (0-0) band emission, however, the self-

absorption process becomes important below ~100 km. As a result, the spectral line shape of any rotational line in (0-0) band emission and the rotational band strucuture will be modified due to variations in extinction from line to line.

Fig.8 shows the computed intensities of all the rotational lines in the O_2 *Atmospheric* (0-0) band at 60 km tangent height with and without considering the self-absorption process. The effect of the self-absorption process is small for the lines near the bandhead and the bandtail whose line strengths are weak, and is large for lines near the band origin. It clearly shows that for some rotational lines, approximately 60-80% of the intensities are absorbed by the molecular oxygen along the line-of-sight.

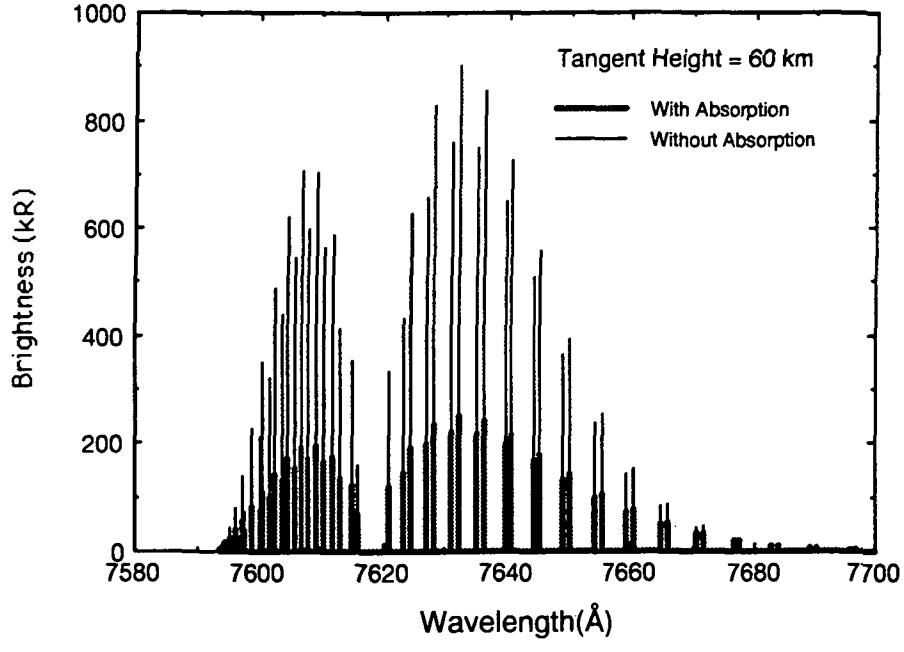

Figure 8. The emission spectra of the O_2 Atmospheric (0-0) band at 60 km tangent height (with and without the effect of self-absorption)

Figure XX presents the intensity as a function of tangent height for four lines of different strengths in the (0-0) band. The variation of the amount of self-absorption with tangent height for each rotational line reflects the variation of the O_2 column density. Hence, by measuring the extinction of the O_2(0-0) band emission intensity as a function of tangent height, one can determine the number density profile of O_2. Figure xx also shows that the effect of self-absorption varies from line to line depending upon its line strength. As the

atmospheric temperature varies, the strength of a given emission line and its absorption cross-section (magnitude as well as line shape) will change accordingly. The knowledge of the atmospheric temperature profile is therefore important in the successful recovery of the O_2 number density. In addtion, the un-attenuated (0-0) band brightness should also be known accurately in order to determine the effective optical depth. This can be accomplished by simultaneously measuring the spectral brightnesses of both optically thin (0-1) and optically thick (0-0) band emissions. The atmospheric temperature profile can be recovered from the rotational structure of the (0-1) band and the un-attenuated (0-0) band brightness is related to the observed (0-1) band brightness by $A_{0\text{-}0}/A_{0\text{-}1}$.

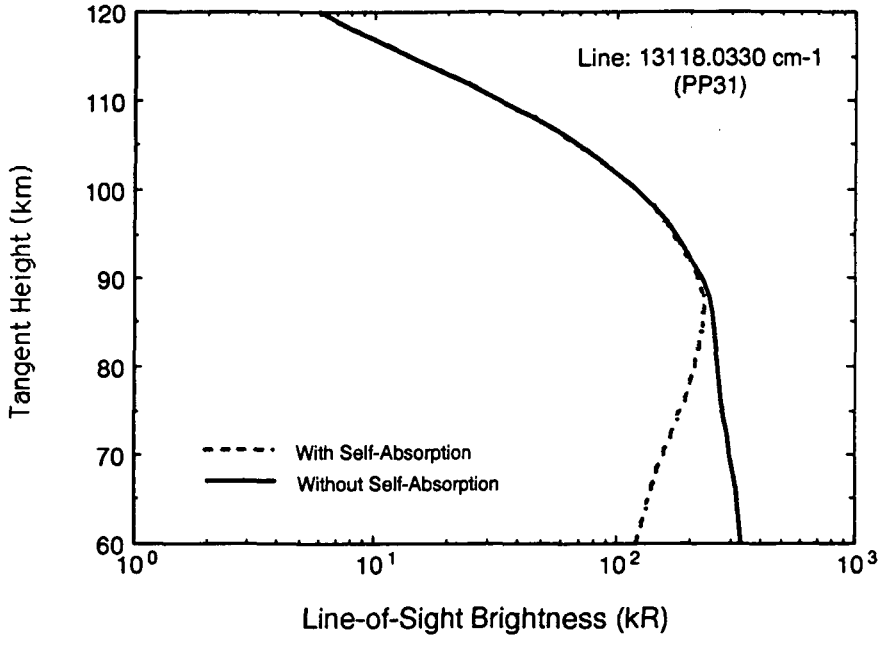

Figure 3.3. The line-of-sight brightness of line PP31 as a function of tangent height (with and without the effect of self-absorption)

Since the $O_2(0,0)$ band is optically thin above 100 km and is ~20 times more intense than the (0,1) band, it provides better temperature measurements in the lower thermosphere. The similarity in O_2 and N_2 mass allows one to extrapolate the N_2 density from the well-mixed mesosphere up to ~160 km with the measured temperature and O_2 density with standard treatments of vertical transport and photochemical induced departures from gravitational diffusive equilibrium (Colegrove et al., 1966; Oran and Strobel, 1976). With the inferred N_2 and measured O_2 densities and temperature, the pressure can be

derived to the accuracy of the ratio of the neglected O density to the sum of the O_2 and N_2 densities.

3.3 Atmospheric Winds

Due to the presence of atmospheric winds, both emission and the absorption cross-section line shapes are doppler shifted. One can recover the atmospheric winds by determining the the amount of doppler shift in the measured line shape. Correction for the motion of the spacecraft should be included if the measurements are conducted from space. This technique has been used for many groundbased doppler measurements and for measurements by the Fabry-Perot Interferometer onboard Dynamic Explorer satellite (Hays et al., 1984, Killeen and Hays, 1984).

Figure xx shows the calculated line shape for the line PP31 of the O_2(0-1) band at 60 km tangent height with and without the influence of atmospheric winds. The line shape with the presence of a wind field which gives rise to a 100 m/sec doppler shift at 60 km and a vertical wind shear of -1 m/sec/km along the line-of-sight is shown for comparison. In general, without wind shear the emission line position is shifted by $\Delta v/c$ with no asymetry in line shape. However, with the presence of wind shear, the line is not only shifted but also asymetric. It is clear from Figure xx that the amount of doppler shift introduced by this reasonably assumed wind field is extremely small ($\Delta v/c = \sim$ cm^{-1}) as compared to the width of the line ($\sim$ cm^{-1}). One has to numerically retrieve this small amount of shift or the effective line-of-sight velocity from either the effective line center position determined from the spectral fit (Killeen and Hays, 1984) or the degree of asymetry around ν_o present in the line shape as indicated in Figure XXX.

The HRDI/UARS instrument is designed in part to retrieve atmospheric wind profile between 55 and 110 km from high resolution line shape measurements of several rotational lines in the O_2 (0-0) band. The analysis becomes more complicated when the rotational lines in the absorption-modified O_2 (0-0) emission band are considered. A method based on the asymetry of the observed line shape around ν_o for the line-of-sight velocity determination and an inversion method derived from the model presented in this paper is employed for HRDI data analysis. The detailed description of the technique and the inversion methods used for HRDI data analysis will be the subject of a subsequent paper.

3.4 $O(^1D)$ and O_3 Number Densities

The major chemical processes in the mesosphere involve rapid interactions between the odd oxygen (O and O_3) and odd hydrogen (OH, H, HO_2) species. O_3 is important because of its role in the radiation (thermal) budget of the atmosphere. The concentration of ozone in this region of the atmosphere has usually been indirectly inferred from the $O_2(^1\Delta)$ 1.27 μm emission produced by the photolysis of O_3 [Thomas et al., 1984]. The $O(^1D)$ atoms are important due to their involvement in the HO_X chemistry, i.e. $O(^1D) + H_2O \rightarrow 2OH$ and $O(^1D) + H_2 \rightarrow H + OH$ and their role in the heat source produced by the quenching collisions. The concentration of $O(^1D)$ atoms in this region is very low, approximately 10^2-10^3 cm^{-3}, and is very difficult to measure using the subsequent radiative emission at 6300Å because of the presence of Rayleigh scattering. As a result, the $O(^1D)$ concentrations used in current model studies in the lower thermosphere and mesosphere are all theoretically calculated based on the photolysis rates of O_2 and O_3.

As it was demonstrated previously, some of the $O_2(^1\Sigma)$ molecules present in the daytime atmosphere are produced by energy transfer reaction of $O(^1D)$ and O_2. Figure xx shows the percentage of $O_2(^1\Sigma)$ molecules produced by various processes described in section 2.1. Above 120 km approximately all of the $O_2(^1\Sigma)$ molecules are produced by reaction involving $O(^1D)$ atoms. This percentage decreases down to ~20% near 80 km as the fluorescence excitation process becomes important. As a result of the production of $O(^1D)$ atoms through photolysis of ozone, $O(^1D) + O_2$ reaction becomes a dominant $O_2(^1\Sigma)$ source again near ~60 km. Mathematically, the production rate of $O_2(^1\Sigma)$ molecules from the $O(^1D)+O_2$ reaction, $P_{O(^1D)+O_2}$, is related to the $O_2(^1\Sigma)$ number density by

$$
\begin{aligned}
P_{O(^1D)+O_2} &= P_{DR} + P_{PE} + P_{SRC} + P_{Ly\text{-}\alpha} + P_{Hartley} \\
&= \beta_{O_2(^1\Sigma)} k[O(^1D)][O_2] \\
&= n_{O_2(^1\Sigma)} (A_{O_2(^1\Sigma)} + k[N_2]) - P_{FE} - P_{3\text{-}body}.
\end{aligned}
$$

Here we have simplified the above equations and considered N_2 as the only $O_2(^1\Sigma)$ quenching species (an excellent approximation in this altitude region). Since the three-body chemical reaction is a minor source, one can determine $[O(^1D)]$ from the measured $[O_2(^1\Sigma)]$ with the knowledge of $[O_2]$ and $[N_2]$ to properly account for the contribution from O_2 fluorescence excitation and the loss of $O_2(^1\Sigma)$ molecules due to quenching. In

addition, since the majority of the $O(^1D)$ atoms below 70 km is produced by photolysis of ozone, one can also derive the ozone concentration based on the solar MUV flux and the O_3 photodissociation cross-section.

3.5 Solar Energy Input and Atmospheric Heating Rates

While the absorption of solar UV radiation by O_2 (SRC) and by O_3 (Hartley band) results in the production of $O(^1D)$ atoms and subsequent $O_2(^1\Sigma)$ molecules, solar energy is also deposited into the atmosphere. The conversion of solar ultraviolet radiation to atmospheric heating involves the transfer of energies among atomic and molecular internal energy, chemical potential energy, and the translational energy (heat). A detailed evaluation of the heating efficiencies has been presented by Mlynczak and Solomon [1993] for numerous solar and chemical processes which are responsible for the generation of heat in the terrestrial middle atmosphere. It is concluded that heating efficiencies for photodissociation of O_2 in SRC and Ly-α spectral region and photolysis of ozone in the Hartley band region are not unity and they can be parameterized for use in the heat budget studies. The recommended heating efficiency paramerizations vary with altitude since they are dependent on the relative competition between quenching (heat release) and radiation. The parameterized heating efficiencies for O_2 SRC and O_3 Hartley band solar heating can be readily applied to solar heating rate calculation and they are indepedent of the photolysis rates and O_2 or O_3 concentration. In addition, since Einstein coefficients are constants and quenching rates depends primarily on $[O_2]$, $[N_2]$ and to a less extent on temperture and [O], Mlynczak and Solomon [1993] concluded that their recommended heating efficiencies are function of pressure only. In other words, if one can measure the O_2 and O_3 photolysis rates as a function of pressure, one can derive the solar heating rate profile using the recommended heating efficiencies parameterized by Mlynczak and Solomon [1993].

As shown previously in Figure xx, the O_2 SRC and O_3 Hartley band photolysis are the main production mechanisms near 110-130 km and below 60 km respectively. The $O_2(^1\Sigma)$ number density at these two altitude regions is directly proportional to the photolysis rate, $J_{SRC}*[O_2]$ or $J_{Hartley}*[O_3]$,

$$n_{O_2(^1\Sigma)} = \frac{\beta_{O_2(^1\Sigma)} k[O_2] J_{SRC}[O_2]}{(A_{\alpha(^1b)} + k[O_2] + k[N_2])(A_{O_2(^1\Sigma)} + k[N_2])} \quad \text{(between 110 and 130 km)}$$

$$n_{O_2(^1\Sigma)} = \frac{\beta_{O_2(^1\Sigma)} k[O_2] J_{Hartley} [O_3]}{(A_{\alpha(^1D)} + k[O_2] + k[N_2])(A_{O_2(^1\Sigma)} + k[N_2])} \qquad \text{(below 60 km).}$$

If one can measure the $O_2(^1\Sigma)$ number density profile from the O_2 Atmospheric band emission in this region, the photolysis rates of O_2 and O_3 can be separately derived based on modeled (or measured) O_2 and N_2 number density profiles and used to calculate the resulting solar heating rates. In addition, since the solar fluxes at SRC spectral region is expected to vary slightly with solar cycle, measurements of $n_{O_2(^1\Sigma)}$ near 120 km can provide not only the atmospheric heating rate, but also a solar SRC proxy if the concentration of O_2 is known.

3.6 Atmosphere Remote Sensing: A summary

In summary, the techniques used for upper atmospheric remote sensing from spectroscopic measurements of $O_2(^1\Sigma)$ dayglow can be separated into two categories. One provides direct measurement of atmospheric state variables (i.e. pressure, density, temperature, and winds) based on the spectroscopic properties of the emissions. The other allows one to derive $[O(^1D)]$, $[O_3]$, solar FUV proxy, and FUV and MUV heating rates from the $O_2(^1\Sigma)$ photochemistry. Figure xxx illustrates an example how measurements of O_2 dayglow emission can be applied for upper atmosphere remote sensing. This remote sensing scheme calls for simultaneous limb measurements of O_2 Atmospheric (0-0) and (0-1) band emission at a medium spectral resolution of ~10-20Å and a vertical spatial resolution of ~1-3 km. From the measured O_2(0-1) rotational structure and band brightness as a function of tangent height one first determines the atmospheric temperature and $O_2(^1\Sigma,\upsilon'=0)$ number density profiles. The temperature profile recovered here is important for the determinations of O_2 number density (emission and absorption line strenghts) and temperature-dependent chemical rate coefficients used in the $O_2(^1\Sigma)$ photochemistry calculation. The $O_2(^1\Sigma,\upsilon'=0)$ number density profile obtained from the (0-1) band can provide the unattenuated O_2(0-0) band brightness necessary for the determination of the amount of self-absorption and ultimately the O_2 number density profile by comparing with simultaneously measured (0-0) band brightness as a function of tangent ray height.

The technique used to derive the $O(^1D)$ density profile relies on accurately accounting for all $O_2(^1\Sigma)$ that is produced by O_2 fluorescence excitation and three-body chemical source.

The contribution from the O_2 fluorescence excitation can be calculated based on the O_2 density (directly involved in the excitation and solar flux attenuation) determined previously and the g-factor (DeMajistre and Yee, 1995). The contribution from the three-body recombination source can be calculated based upon an atomic oxygen density profile from a model (such as the MSIS 90) and atmospheric density (directly involved in the production and quenching reactions) and temperature (indirectly involved through the temperature dependence of rate coefficients). By subtracting the contributions by these two production mechanisms from the measured $O_2(^1\Sigma)$ number density, one can determine the $O_2(^1\Sigma)$ production rate by $O(^1D)+O_2$ and consequently deduce the $O(^1D)$ density profile. It should be noted here that the contribution from the three-body source is very small compared to the rest of the sources and the effect of not accurately knowing the atomic oxygen density is insignificant.

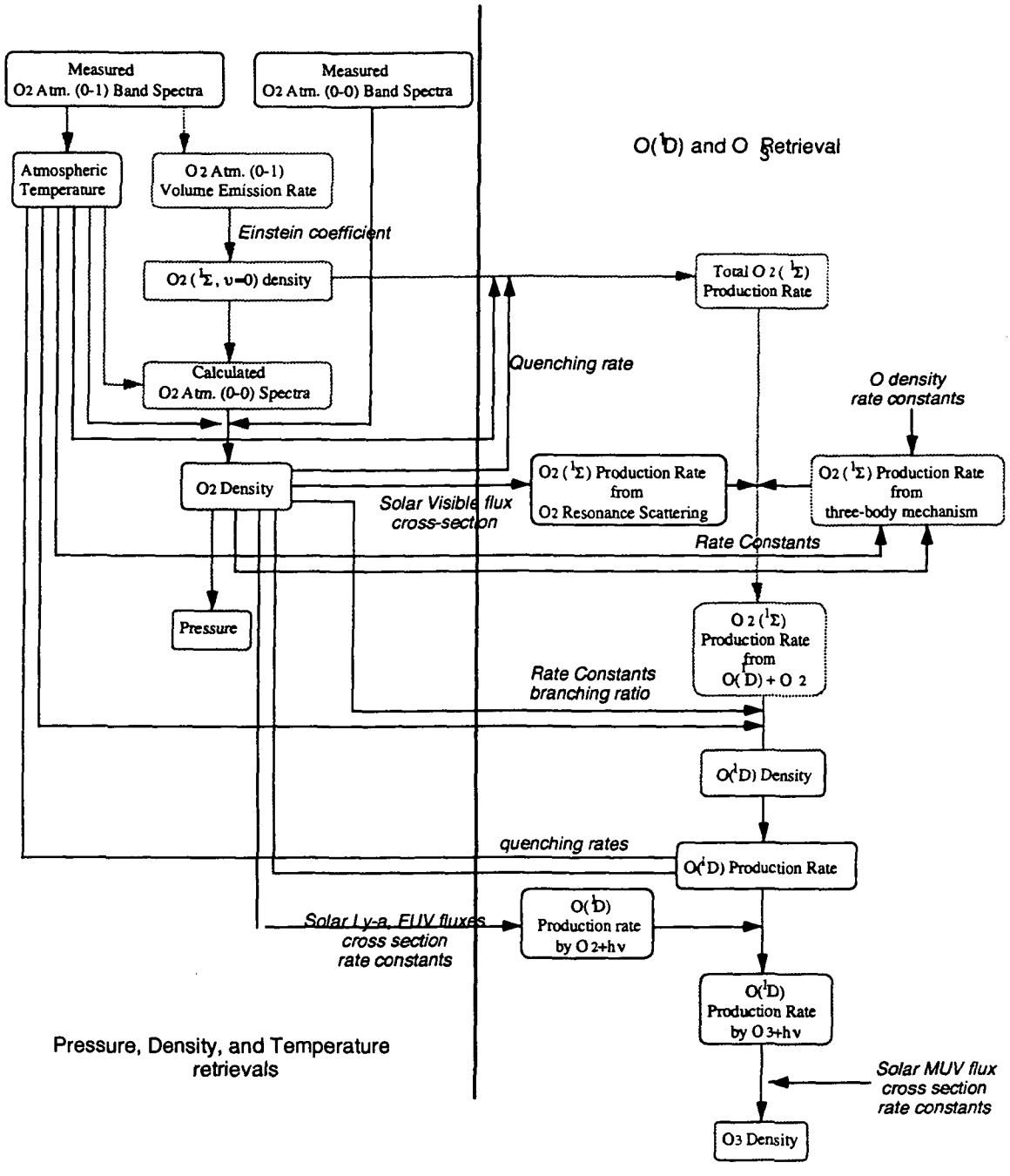

Figure xxx Upper Atmosphere Remote Sensing Using $O_2(^1\Sigma)$ Dayglow

Similarly, the method used to calculate the O_3 density profile relies on accurately accounting for all $O(^1D)$ that is produced by O_2 photodissociation and O_3 photolysis. To determine the contribution from the O_2 photodissociation source, one needs not only the O_2 number density profile, but also the simultaneous solar SRC and Ly-α fluxes. If measured solar flux is not available, one can used the solar SRC flux proxy determind

from the $O_2(^1\Sigma)$ number density around 110-130 km and an F10.7 scaled Ly-α flux used widely by the community (Torr and Torr, 1979; Solomon and Abreu, 1984). Once the O_3 photolysis rate profile is isolated, one can easily retrieve the O_3 number density profile since the solar MUV flux does not expect to vary very much with solar activity and has been measured previously (c.f. Lean, 1992).

It should be noted that the energy transfer efficiency from $O(^1D)$ to O_2 in the $O(^1D)+O_2$ reaction is a very important parameter in the above remote sensing scheme. Lee and Slanger [1978] reported a value of 0.77 ± 0.23, implying that approximately 30% systematic error could be present in the recovered $O(^1D)$ and O_3 number density profiles. Further laboratory and aeronomical determinations on this critical parameter are needed in order to properly interprete measurements of $O_2(^1\Sigma)$ in terms of $O(^1D)$ and O_3.

4. SUMMARY AND DISCUSSION

The $O_2(^1\Sigma)$ Atmospheric band emission is one of the brightest airglow features observed from space and extends an altitude region between ~50 and 200 km. The emission is produced by photochemical reactions and fluorescence excitation process which involve solar EUV, FUV (SRC), MUV (Hartly band), and visible (~685nm and 765nm) photons and atmospheric major (O, O_2, N_2) and minor ($O(^1D)$, O_3) species. Each of the emission bands of this system covers approximately 200Å with its shape determined by the atmospheric temperature. The spectral line shape of any rotational line in these bands can also be doppler-shifted due to the presence of atmospheric motion. In addition, at tangent height below 100 km, the spectral brightness of the (0-0) band emission is affected by the self-absorption process and the O_2 number density along the line of sight. Consequently, the O_2 Atmospheric band emissions contain tremendous amount of information about the vertical structure of the atmosphere (i.e. temperature, winds, and O_2 number density) and the external solar energy input.

We have pointed out that one may require the knowledge of many atmospheric and necessary spectroscopic and kinetic parameters in order to properly interpret the measured $O_2(^1\Sigma)$ spectral brightness and its photochemistry. Table 4.1 gives the summary of the important parameters required for an accurate upper atmospheric remote sensing. One needs to carefully examine the accuracies of all the atmospheric parameters (i.e. either measured or assumed) and the spectroscopic and kinetic parameters required in order to assess the statistical and systematic uncertainties in the retrievals. For example, in order to retrieve O_2 number density profile from the amount of self-absorption in the (0-0) band emission, one has to know not only the unattenuated (0-0) band emission brightness, but also the atmospheric temperature profile and absorption cross-section. To retrieve the O_3 density profile from an $O_2(^1\Sigma)$ band volume emission rate profile, one needs to know additional geophysical parameters such as O_2, N_2, O number densities, atmospheric temperature, solar fluxes, and some kinetic and spectroscopic parameters such as rate coefficients, branching ratios, and cross-sections, etc. Of course, a detailed accounting for all sources and sinks of $O_2(^1\Sigma)$ molecules is also required. Figure x illustrates the solar/atmospheric parameters that affect the spectral brightness of the O_2 Atmospheric band emissions and how the variation of each parameter affects the observed band brightness. It demonstrates the altitude region where the information of one particular solar/atmospheric parameter resides and the relative importance of knowing other required

parameters. In principle, the accuracy of any recovered geophysical parameters depends

Table 4.1 Required parameters for upper atmospheric remote sensing using $O_2(^1\Sigma)$ dayglow emissions

Recovered Geophysical Parameters	Required Parameters
O_2 number density (50-120 km)	O_2(0-0) band spectral brightness; O_2(0-1) band spectral brightness; temperature; O_2 absorption cross section;
Temperature (50-180 km)	$O_2(^1\Sigma)$ band volume emission rates; O_2 number density (for 0-0 band only);
Wind (50-180 km)	$O_2(^1\Sigma)$ band emission rates; temperature; O_2 number density (for 0-0 band only);
$O(^1D)$ number density (50-120 km)	O_2 number density; $O_2(^1\Sigma)$ volume emission rates; g-factors (for both 685 nm and 760 nm); O number density; temperature; $A_{O_2(^1\Sigma)}$, k_5, k_6; k_1, k_2, $\beta_{O_2(^1\Sigma)}$, $A_{^1D}$;
O_3 number density (50-100 km)	$O(^1D)$ number density; O_2 number density; Solar Ly-α, FUV and MUV fluxes; O_3 Hartley band cross section and β_2; O_2 SRC cross section; O_2 Ly-α cross section and β_1; temperature; k_1, k_2,$A_{^1D}$;
direct O_2 SRC heating rates	O_2 (and N_2) number density; Solar FUV fluxes; temperature;
direct O_3 heating rates	O_3 number density; O_2 (and N_2) number density; Solar MUV fluxes; temperature;
$O(^1D)$ heating rates	$O(^1D)$ number density; O_2 (and N_2) number density; k_1, k_2, $\beta_{O_2(^1\Sigma)}$; temperature.

parameters. In principle, the accuracy of any recovered geophysical parameters depends on not only the accuracies of the required solar/atmospheric parameters, but also the kinetic/spectroscopic parameters listed in Table 4.1. The theoretical model presented here will allow us to examine each required parameter and its contribution to the final error budget of the recovered parameter. The exact algorithms, inversion methods, and

sources of errors of the remote sensing technique shown here are beyond the scope of this paper and will be addressed in details in subsequent papers when each of these remote sensing applications is applied.

Acknowledgment

NASA Rocket Grants, AFGL grants, HRDI grant, and MSX.

Thanks to Paul B. Hays, Vincent Abreu, W. R. Skinner, Stan Solomon,Frank Marcos.

REFERENCES

Allen, M., A new source of ozone in the terrestrial upper atmosphere? J. Geophys. Res., 91, 2844, 1986.

Babcock and Herzberg, 1948.

Bevilacqua, R. M., D. F. Strobel, M. E. Summers, J. J. Olivero and M. Allen, The Seasonal Variation of Water Vapor and Ozone in the Upper Mesosphere: Implications for Vertical Transport and Ozone Photochemistry, J. Geophys. Res. 95, 883, 1990.

Broadfoot, 1994.

Bucholtz, A., W. R. Skinner, V. J. Abreu, and P. B. Hays, The Dayglow of the O_2 Atmospheric Band System, Planet. Space Sci., 34, 1031, 1986.

Chamberlain, et al, 1954.

Clancy, R. T., D. W. Rusch, R. J. Thomas, M. Allen, and R. S. Eckman, Model Ozone Photochemistry on the Basis of Solar Mesosphere Explorer Mesospheric Observations, J. Geophys. Res., 92, 3067, 1987.

Deans et al., 1976;

DeMajistre and Yee, 1995.

Gauthier, M. and Snelling, D. R., Formation of singlet molecular oxygen from the ozone photochemical system, Chem. Phys. Lett., 5, 93, 1970.

Gauthier, M. and Snelling, D. R., Mechanisms of singlet molecular oxygen formation from photolysis of at 2357Å, Chem. Phys. Lett., 54, 4317, 1971).

Hays et. al, 1992 HRDI

Hedin, MSIS, 1990

Heller et al., 1987.

Lee, L. C., and T. G. Slanger, Observations on $O(^1D \rightarrow ^3P)$ and $O_2(b^1\Sigma_g^+ \rightarrow X^3\Sigma_g^-)$ following O_2 photodissociation, J. Chem. Phys., 69, 4053,1978.

Lopez-Gonzales et al., 1992.

McDade et al., 1986

Meinel, 1950.

Meinel, 1951.

Meriwether, 1991.

Mlynczak, M. G. and S. Solomon, A Detailed Evaluation of the Heating Efficiency in the Middle Atmosphere, J. Geophys. Res. 98, 10517, 1993.

Mlynczak, M. G., S. Solomon and D. S. Zaras, An Updated Model for $O_2(a^1\Delta_g)$ concentrations in the Mesosphere and Lower Thermosphere and Implications for Remote Sensing of Ozone at 1.27 μm, J. Geophys. Res. 98, 18639, 1993.

Packer, D. M., Altitudes of the night airglow radiations, Ann. Geophys., 17, 67, 1961.

Schmidtke et al., 1992

Skinner and Hays, 1985.

Slanger, T. G. Vibrational excitation in $O_2(b^1\Sigma_g^+)$, Can. J. Phys., 64, 1657, 1986.

Slanger, T. G., E. J. Llewellyn, I. C. McDade, and G. Witt, Comment on "The O_2 Atmospheric Dayglow in the Thermosphere" by M.R. Torr, B. Y. Welsh, and D. G. Torr, J. Geophys. Res. 92, 7753, 1987.

Solomon, S. C. and V. J. Abreu, The 6300Å Dayglow, J. Geophys. Res., 1984.

Thomas, R. J. Seasonal Ozone Variations in the Upper Mesosphere, J. Geophys. Res., 95, 7395, 1990.

Torr, M. R., B. Y. Welsh, and D. G. Torr, The O_2 atmospheric dayglow in the thermosphere, J. Geophysics Res., 91, 4561, 1986.

Wallace, L. and J. W. Chamberlain, Excitation of O_2 Atmospheric bands in the Aurora, Planet. Space Sci., 2, 60, 1959.

Wallace, L. and D. M. Hunten, Dayglow of the Oxygen A Band, J. Geophys. Res., 73, 4813, 1968.

Wanahabe, 1964.

White, 1977

Witt et al., 1979;

Yee et al., 1992.

Yee et al., 1992

Yee et al., 1993.